https://doi.org/10.5194/egusphere-2026-1650
Preprint. Discussion started: 16 April 2026

The evolution of cloud microphysical properties during Cold Air Outbreaks - a composite approach to in situ measurements

Nina E. Larsgård[1], Tim Carlsen[1], Robert O. David[1], Filip Severin von der Lippe[1], Alfons Schwarzenboek[3], Harald Sodemann[2], and Trude Storelvmo[1]

[1]Department of Geosciences, University of Oslo, Oslo, Norway
[2]Geophysical Institute, University of Bergen, Norway
[3]Laboratoire de Météorologie Physique (LaMP), UMR 6016, Université Blaise Pascal, CNRS, Clermont-Ferrand, France

Correspondence: Nina E. Larsgård (n.e.larsgard@geo.uio.no) and Robert O. David (r.o.david@geo.uio.no)

Abstract. When cold, dry polar air is advected over a warmer ocean, a rapid development of clouds is observed. Several airborne field campaigns have been dedicated to these marine Cold Air Outbreaks (mCAOs). However, their properties, as well as their impact on the energy budget and water cycle, remains poorly understood. This study investigates the evolution of cloud microphysics during mCAOs through use of airborne in situ observations of ice crystals and water droplets from a recent Spring campaign in the Norwegian Sea (ISLAS2022). As individual flights only offer snapshots into certain parts of the mCAO evolution, a composite approach has been developed that integrates the in situ microphysical observations from multiple flights in order to capture the entire mCAO development. Thin, low ice clouds were observed over sea ice, reaching cloud top altitudes around 1200 m high. A rapidly developing "stratiform" region has been observed, where liquid-topped mixed-phase clouds increase in vertical extent, as the boundary layer deepens with increasing distance from the sea ice edge. At around 600 km fetch, rapid glaciation in a subsequent "convective" region leads to deep (up to 4500 m cloud top), almost completely glaciated, precipitating clouds that are reaching the end of their lifetime. While the observed microphysical properties are in agreement with earlier studies, the study highlights the potential of the composite approach in moving away from individual case studies to a more holistic microphysical picture of mCAOs, especially when statistics are improved by including additional campaign datasets in the future.

1 Introduction

The Arctic is experiencing an accelerated warming compared to other parts of the world (so-called Arctic amplification) (Serreze and Barry, 2011; Pithan and Mauritsen, 2014; Forster et al., 2021). It is believed that Arctic clouds play a crucial role in this amplified climate response through complex feedback loops involving aerosol-cloud-precipitation-radiation interactions (e.g., Taylor et al. (2022); Wendisch et al. (2023)). This is due to the sensitive balance between liquid and ice in Arctic mixed-phase clouds (MPCs, between 0 and -38 °C), which exerts a strong control on the Arctic energy budget (Shupe and Intrieri, 2004; Mioche et al., 2015; Tan and Storelvmo, 2019), precipitation formation, cloud lifetime, and radiative properties (Morrison et al., 2012; Andronache, 2017). Thus, characterizing the cloud phase distribution in Arctic MPCs and identifying

https://doi.org/10.5194/egusphere-2026-1650
Preprint. Discussion started: 16 April 2026

exactly how the cloud phase balance will change in the future are central to understanding how clouds affect Arctic climate and vice versa (Forster et al., 2021).

A large fraction of Arctic MPCs are associated with marine cold air outbreaks (mCAOs) during Arctic winter (Dahlke et al., 2022). mCAOs are characterized by very cold, dry air originating from ice- and snow-covered regions being advected over the relatively warmer open ocean. This results in a rapid development of clouds, often associated with extreme weather events such as heavy precipitation, strong winds and even polar lows (Landgren et al., 2019; Kolstad, 2017). The mCAO index M is a measure of the strength of the mCAOs and is defined as the difference between the potential temperatures at the sea surface θ_{SST} and at 850 hPa θ_{850} (Papritz et al., 2015; Fletcher et al., 2016):

$$M = \theta_{\mathrm{SST}} - \theta_{850} \tag{1}$$

Following Papritz and Spengler (2017), mCAOs are classified as weak if $M < 4\,\mathrm{K}$, moderate if $M < 4 - 8\,\mathrm{K}$, strong if $M < 8 - 12\,\mathrm{K}$ and very strong if $M > 12\,\mathrm{K}$.

During mCAOs, when air moves off sea ice over open ocean, an abrupt increase in instability and heat and moisture fluxes (Pithan and Mauritsen, 2014; Geerts et al., 2022; Lackner et al., 2023) leads to convection, a deepening of the boundary layer and the development of a stratocumulus layer. The clouds then organize as "streets", horizontal convective rolls caused by wind shear in the boundary layer due to heating from below (Young et al., 2002). These relatively shallow clouds have well-defined boundaries, meaning that limited lateral mixing occurs in these air masses (Pithan et al., 2018).

As the mCAO cloud field develops further, it breaks up into more cellular structures and deepens into cellular cumulus or even cumulonimbus clouds (Brümmer, 1996). One proposed reason for this break-up is that the wind shear weakens with increasing fetch, allowing the vertical mixing to become more important for the organization of the clouds (Saggiorato et al., 2020; Juliano et al., 2024). Increased precipitation has also been shown by some studies (Torri et al., 2015; Abel et al., 2017; Pithan et al., 2018; Juliano et al., 2024) to be a contributing factor to the transformation from stratiform cloud streets to convective cells. With increasing precipitation, the air below the clouds is cooled by evaporating or sublimating precipitation, creating cold pools that cut off the updraft. Consequently, the source of moisture for droplet generation is also cut off, resulting in cloud cells becoming completely glaciated and eventually dissipating through precipitation. At the same time, gust fronts collide and initiate further convection and new generation of clouds. The combination of these two processes are responsible for the open, cellular structure of the clouds (Tornow et al., 2021; Saggiorato et al., 2020).

Lackner et al. (2024) and Juliano et al. (2024) characterized the early-development of mCAO clouds consisting of stronger updrafts, larger amounts of liquid water, lower cloud tops, and less precipitation than the more mature mCAO clouds. Liquid-topped MPCs are frequently observed during the early stages of mCAO development over open ocean (Young et al., 2016; Gayet et al., 2007; Ruiz-Donoso et al., 2020). Abel et al. (2017) observed a decrease in cloud droplet number concentration (CDNC) as mCAO clouds transition from stratocumulus streets to open cells. This depletion of liquid has been linked to increased ice production (Karalis et al., 2022) and precipitation as the mCAO clouds mature and start to decay. Decaying mCAO clouds are characterized by weaker updrafts and lower liquid water content (LWC) (Lackner et al., 2023, 2024). Murray-Watson

https://doi.org/10.5194/egusphere-2026-1650
Preprint. Discussion started: 16 April 2026

et al. (2023) and Murray-Watson and Gryspeerdt (2024) used satellite observations of mCAOs to investigate the transition from stratiform cloud streets to open cells as a function of the time since sea ice. They found that precipitation is important for initiating the transition from stratiform cloud streets to open cells, and also pointed out the potential for aerosol changes to affect this transition. A comprehensive understanding of mCAO evolution and associated microphysical properties is a prerequisite to predict how mCAO clouds might change in response to a rapidly warming Arctic.

The complete evolution of mCAO clouds can span 1000 km, while the processes controlling their development occur on a wide range of scales down to the micrometer scale for microphysical processes. This wide range of scales means that comprehensively observing the development of mCAO clouds is a challenge. Airborne in situ measurements offer a high degree of detail for the small-scale microphysical properties and are therefore invaluable for understanding the small-scale processes in mCAOs. However, the airborne in situ measurements of mCAO clouds are limited for a number of reasons, including aircraft range, cost, and the remote and harsh sampling area in the Arctic. This also means that the observations typically come from a limited number of mCAO events and from individual flight case studies that only offer snapshots into certain parts of the mCAO evolution.

This study aims to investigate the entire cloud microphysical evolution during mCAOs from the sea ice to the Norwegian Coast. For this purpose, a novel composite approach was developed that integrates in situ microphysical observations from multiple flights as a function of the distance from the sea ice edge (fetch). This study uses airborne in situ observations from the ISotopic Links to Atmospheric water's Sources (ISLAS2022, see Sodemann (2026), in prep) field campaign, in order to characterize the evolution of mCAO clouds by means of the measured size-resolved liquid droplet and ice crystal number concentrations and subsequent derived quantities (liquid and ice water content, effective radii, supercooled liquid fraction).

Section 2 establishes the airborne cloud microphysical measurements during ISLAS2022: Relevant instrumentation and the data selection criteria used in this study are presented, and then the composite approach is introduced. Section 3 investigates the microphysical development of mCAO clouds encountered during ISLAS2022 as a function of the fetch, before we put our findings into context in Section 4.

2 Methods

2.1 ISLAS2022 research flights

The in situ measurements used in this study were gathered during the ISLAS2022 field campaign (see (Sodemann, 2026), in prep for more details) between 21 March 2022 and 10 April 2022.

Nine research flights were utilized with flight tracks over the Norwegian Sea between Kiruna in Northern Sweden and Longyearbyen (Flights IS22-02 to IS22-11, thereby excluding flight IS22-09, which was ultimately performed over land). An overview of the flight tracks of the ISLAS2022 flights utilized in this study - all targeting mCAO situations - is given in Fig. 1 together with the maximum (3 April) and minimum (22 March) sea ice extent observed throughout the campaign.

The well-recognized cloud pattern of a typical mCAO is best seen from satellite: Figure 1b) shows an exemplary flight path for the flight IS22-07 (29 March 2022) on top of a collocated MODIS satellite image. It (a) demonstrates nicely the dense

https://doi.org/10.5194/egusphere-2026-1650
Preprint. Discussion started: 16 April 2026

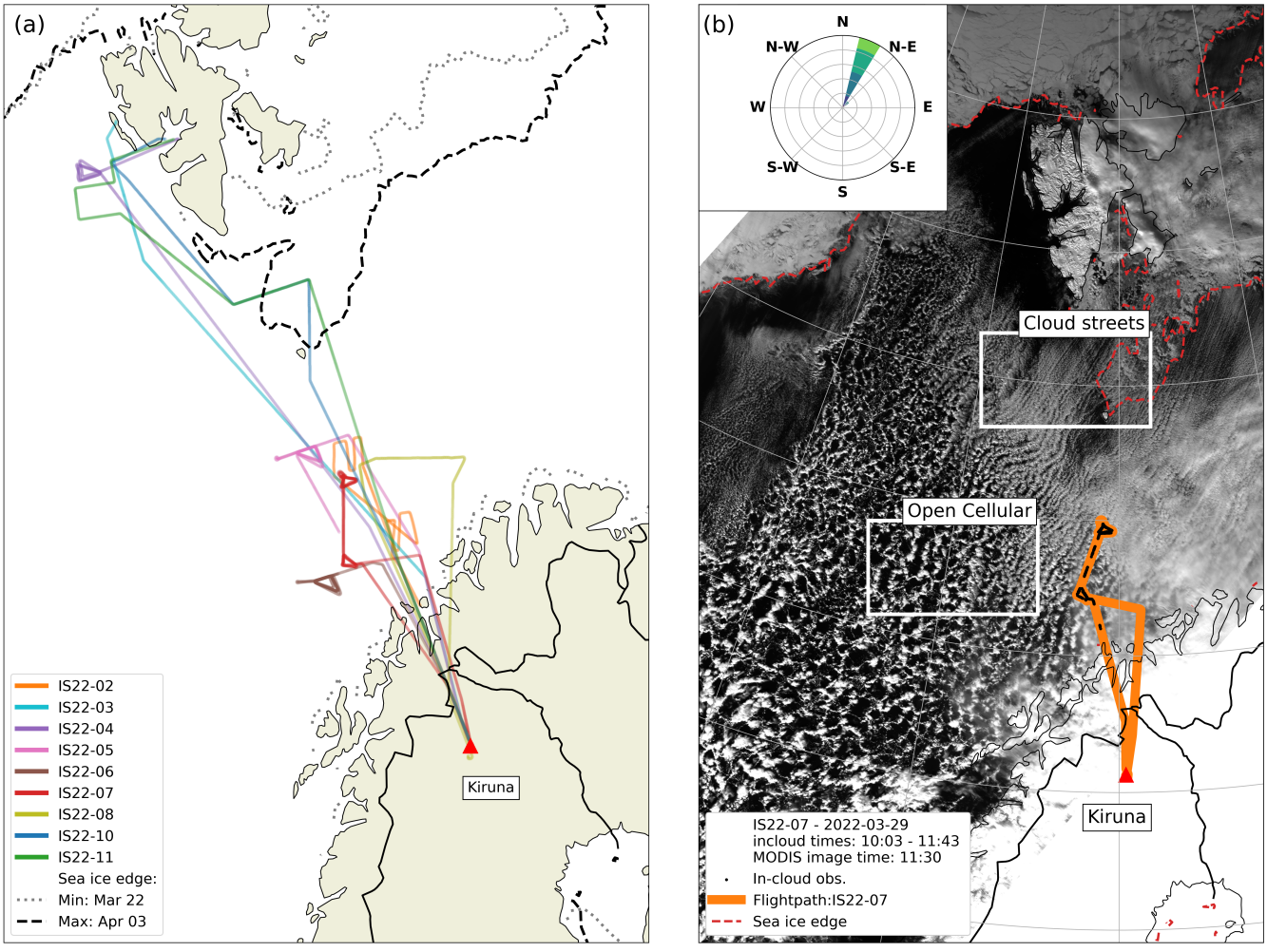

Figure 1. (a) Overview of flight tracks (color-coded) used in this study from the ISLAS2022 campaign out of Kiruna, Sweden. Maximum (dashed) and minimum (dash-dotted) sea ice extent throughout the campaign are shown in gray. (b) Exemplary MODIS image (Band 1: 620-670 nm wavelenght band) during flight IS22-07 to illustrate the mCAO situations commonly sampled throughout the campaign. In addition to the flight track (orange), the sea ice edge (red dashed line), wind rose for the wind direction along the flight track (top left), and example areas of mCAO cloud streets and open cells (white boxes) are shown.

cloud streets located just downwind of the sea ice edge and a gradual transition into an open, cellular structure with increasing fetch, and (b) puts the in-cloud measurements during that flight (black) into context, as the aircraft was flying in the transition zone, where the denser cloud streets gradually broke up into more open cellular convection.

Table 1 gives details for the flights used in this analysis, including the covered distances from the sea ice edge and the mCAO index M (see Sect. 2.3 for details). Maps showing the spatial distribution of the mCAO index and the corresponding flight tracks for each of the ISLAS2022 flights can be found in Figures A3 to A11 in Appendix A. Overall, the ISLAS flights

https://doi.org/10.5194/egusphere-2026-1650
Preprint. Discussion started: 16 April 2026

Table 1. Overview of the ISLAS2022 flights, including details of in-cloud properties. The mCAO index M is given as the median value along the flight track.

Flight	Date	Wind direction	# 5s samples	Max and min fetch	Median mCAO index M	mCAO category
IS22-02	2022-03-22	W	1405	[825 km – 1000 km]	5 K	Moderate
IS22-03	2022-03-24	N	192	[125 km – 200 km]	8 K	Moderate
IS22-04	2022-03-24	N	461	[25 km – 275 km]	14 K	Very Strong
IS22-05	2022-03-26	NNW,N	581	[350 km – 525 km]	10 K	Strong
IS22-06	2022-03-26	NNW	560	[600 km – 875 km]	8 K	Moderate
IS22-07	2022-03-29	NNE	547	[325 km – 725 km]	6 K	Moderate
IS22-08	2022-03-30	NNE	254	[450 km – 575 km]	5 K	Moderate
IS22-10	2022-04-03	NE	523	[-125 km – 150 km]	7 K	Moderate
IS22-11	2022-04-03	NE, ENE	790	[-125 km – 225 km]	7 K	Moderate

used in this analysis covered moderate to very strong mCAOS (median values of M given in Table 1). The main wind direction had a strong northerly component for all flights except the first (IS22-02), where the main wind direction was westerly. The westerly winds during this flight led to cloud observations at the farthest distances from the sea ice edge (1125 km) measured during the campaign. In addition, the two flights IS22-10 and IS22-11 (3 April 2022) sampled clouds over the sea ice. Thus, in-cloud observations ranged from fetch values of -125 km to 1000 km.

2.2 In situ suite of cloud microphysical instruments

The French SAFIRE ATR42 research aircraft (ATR) used during ISLAS2022 was equipped with a suite of in situ cloud microphysical instruments including a Cloud Droplet Probe (CDP, a forward-scattering optical spectrometer) and a Cloud Imaging Probe (CIP). Both instruments were mounted on the ATR aircraft during the ISLAS2022 campaign illustrated Fig. 2a.

The aircraft was also equipped with a standard suite of instruments for measuring meteorological parameters such as temperature, humidity, pressure, and wind. This includes a Rosemount sensor that provided the temperature observations that were used in our analysis.

2.2.1 Post-processing of CDP

The CDP, manufactured by Droplet Measurement Technologies, is a forward-scattering optical probe that counts and sizes particles. While the particles pass through a laser beam in the instrument, the intensity of the light scattered into the forward direction is eminently dependent on its particle size (DMT, 2017). The 30 size bins of the CDP span particle sizes from 3 µm to 50 µm, which mainly covers cloud droplets and larger aerosol particles (Fig. 2b). The lower sizing bins of the CDP may

https://doi.org/10.5194/egusphere-2026-1650
Preprint. Discussion started: 16 April 2026

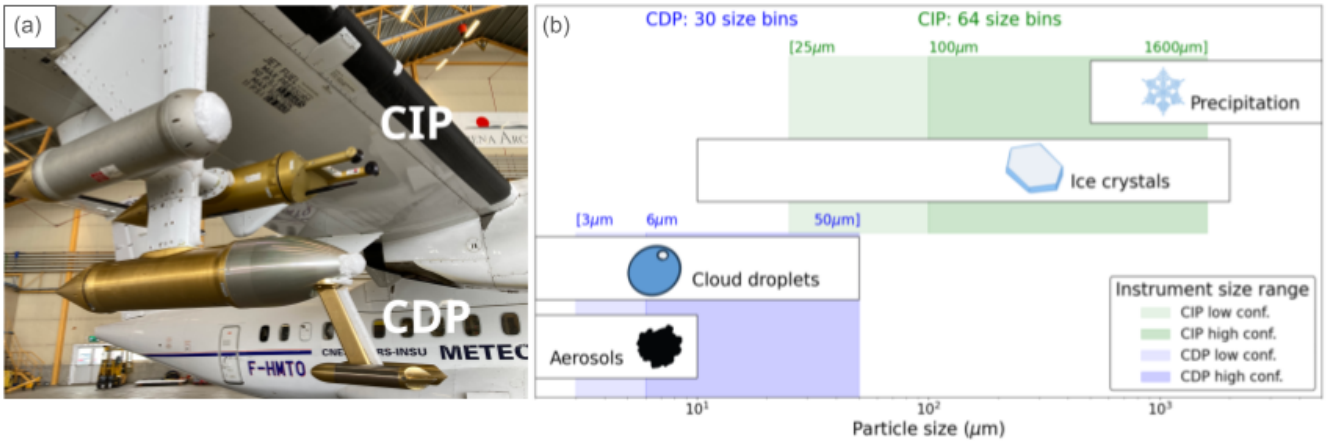

Figure 2. Microphysical instrumentation during the ISLAS2022 campaign. (a) The CDP and the CIP mounted on the ATR aircraft. (b) Cloud particle size ranges (and corresponding types) detectable with the CDP and the CIP.

have a higher uncertainty, as they might be more affected by shattering effects, electronic noise and coincidence. Therefore, All subsequently derived parameters from the CDP measurements are calculated using the size bins of 6 µm and larger.

Cloud droplet number concentration (CDNC): The total CDNC per time step was calculated by summing the particle count p_i per bin i for all the bins used (bin 3 corresponding to 6 µm), and dividing it by the sample volume SV (see Eq. 2).

$$\mathrm{CDNC}(t) = \frac{\sum_{i=3}^{30} p_i(t)}{\mathrm{SV}(t)} \tag{2}$$

SV for the CDP (and for the CIP) depends on the speed of the aircraft relative to the air, which is called the True Air Speed (TAS). The TAS is calculated from dynamic and static pressures measured with pitot probes at the front of the fuselage. The sample volume for a given timestep Δt is the collected sample area (SA) of the instrument [0.269 mm^2] multiplied by the TAS: $\mathrm{SV}(t) = \mathrm{SA} \times \mathrm{TAS} \times \Delta t$.

Liquid Water Content (LWC): The LWC per timestep Δt is found by calculating the mass of the droplets in each size bin. By assuming all droplets are spherical, the mass is found using the volume of a sphere with radius r_i multiplied with the density of water ρ_w=1000 $\mathrm{kg\,m^{-3}}$. By integrating over the particle size distribution, the total LWC is found. For the LWC used in this analysis the integration is done over the size bins that exceeds 6 µm.

Effective Diameter (ED): We use ED as the sizing parameter for the cloud droplets observed by the CDP. The ED represents the average cloud droplet size weighted by area. This parameter (or its sister parameter effective radius) is often used in radiative transfer calculations and climate modeling due to the close connection between this parameter and the radiative properties of clouds (Mitchell et al., 2011; Peng et al., 2002). The ED for each timestep t was calculated with the following equation where p_i is the particle count for bin i, and r_i is the respective radius of the cloud droplets in this bin:

https://doi.org/10.5194/egusphere-2026-1650
Preprint. Discussion started: 16 April 2026

$$\mathrm{ED}(t) = \frac{\sum_{i=3}^{30} p_i(t) \cdot r_i^3(t)}{\sum_{i=3}^{30} p_i(t) \cdot r_i^2(t)} \cdot 2 \tag{3}$$

2.2.2 Post-processing of CIP

The CIP optical array probe measures the particles as they occlude a collimated laser beam projected onto a linear array of 64 photodiodes, thereby capturing two-dimensional shadow images of the cloud particles (Baumgardner et al., 2011, 2001). The 64 size bins of the CIP range from 25 µm to 1600 µm. These sizes target mainly ice crystals and small precipitation particles (see Fig. 2b). Previous studies have found that larger cloud particles are generally ice in Arctic MPCs (e.g. Korolev et al. (2017); McFarquhar et al. (2007)). We therefore assume that cloud particles measured by the CDP are liquid droplets, and cloud particles measured by the CIP are ice crystals when temperatures are below freezing and above the homogeneous freezing temperature. Despite the theoretic overlap in the sizes measured by the CDP and the CIP between 25 µm and 50 µm, this study only considers CIP particle sizes of 100 µm or larger. This is due to the well-known limitation of the CIP where the smallest sizing bins are prone to undercounting and mis-sizing because of depth of field and optical resolution(Korolev et al., 1998). In order to have confidence in the size of the particles measured by the CIP, the particles should cover at least 3 photodiodes (Korolev et al., 1998; de Reus et al., 2009). Cloud droplets also dominate the number concentration of the smaller particles, so any ice crystals in the smaller sizes will not significantly influence liquid/ice phase estimates.

Fig. 3 shows examples of images acquired by the CIP, which are then processed with the SODA2 software for OAP Data Analysis (Bansemer, 2016). This software processes raw images from OAPs, creates particle size distributions, and calculates parameters such as area ratio and aspect ratio. The TAS is used in the processing to calculate the sample volume and the particle sizes depending on the sizing method used. In this case we used the circle-fit method (e.g. Wu and McFarquhar (2016)), which uses the diameter of the smallest circle that encompasses the particle as the particle size. As this method requires the entire particle to be imaged, all partially detected particles i.e. any truncated particles is removed ("all-in" correction from Heymsfield and Parrish (1978)). Particles rejected with this method are exemplified by particles A, B and D in Fig. 3. Of course, this all-in method eliminates observations of large snow particles, which where frequently sampled below cloud base. To remove artifacts from particle shattering on the tips of the instrument (Korolev et al., 2013), an inter-arrival time rejection method following (Field et al., 2006) was applied together with a 5 s integration time that allows for sufficient particle statistics. Particle C in Fig. 3 is an examples of smaller particles from a shattering event that is rejected with this method.

After applying these corrections, we use the SODA2-calculated parameters; number concentration, particle size and ice water content.

Ice Crystal Number Concentration (ICNC): The ICNC is calculated within the SODA2 program as the CIP total number concentration of ice crystals beyond 100 µm.

Ice Water Content (IWC): The IWC is calculated using the mass-dimension parameterization from Brown and Francis (1995):

https://doi.org/10.5194/egusphere-2026-1650
Preprint. Discussion started: 16 April 2026

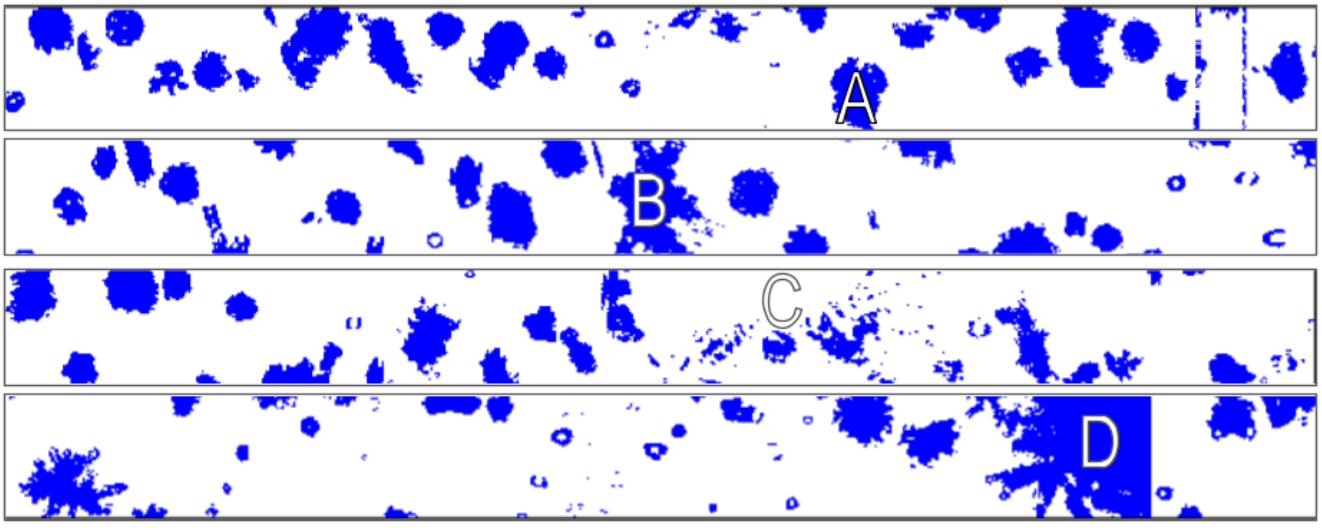

Figure 3. Sequence of raw CIP images with examples of particles before applying artefact removal (shattering out if focus, all-in, etc.). Example from flight IS22-10. Letter (A) represents a particle that is truncated on one side of the linear photodiode array, letter (B) shows a particle that is truncated on both sides, letter (C) is an example of a shattered particle probably after impact on the instrument tips, and letter (D) shows a particle that is also cut off in the flight track direction, due to its size.

$$m(D_i) = a(D_i)^b \tag{4}$$

Here m is the particle mass in grams, D is the particle diameter in microns for bin number i, and the coefficient $a = 0.0294$ and coefficient $b = 1.9$. The particle diameter D was determined by the circle fit method in SODA2. The diameter determined by this method is the diameter of the smallest circle that enclose the particle image.

The Brown-Francis mass-parametrization was established based on cirrus measurements, and does not give reliable masses for smaller ice particles. However, this parametrization is used in this study which is solely using crystals with diameters beyond 100 µm.

This mass can then be multiplied by particle count p_i for all the size bins used (in our case size bin 3 to 64), in order to estimate IWC:

$$\mathrm{IWC}_{100}(t) = \sum_{i=3}^{64} p_i m(D_i)(t) \tag{5}$$

It should be noted that the parameterization from Brown and Francis (1995) was developed for mid-latitude cirrus clouds, which means that the IWC is likely underestimated for (heavily) rimed particles.

https://doi.org/10.5194/egusphere-2026-1650
Preprint. Discussion started: 16 April 2026

Median Volume Diameter (MVD): We use the MVD as the sizing parameter for the ice crystals, which is defined as the diameter that divides the size distribution in two equal parts (50 %) of total water content. Due to their complex shape, the connection between ED and the radiative properties is less pronounced for ice crystals (Wyser and Yang, 1998; Mitchell et al., 2011), which is why we decided to use MVD. This is justified as we are not comparing the sizes of liquid droplets (ED) and ice crystals (MVD) directly but rather investigate their development as the mCAO evolves.

As for the other CIP parameters, the version of MVD used in this analysis is the one calculated by SODA2 for bins of size equal to or larger than 100 µm, equivalent to removing the first 3 sizing bins.

2.2.3 Derived cloud properties

Combining the CDP and CIP measurements, we further define the total water content and supercooled liquid fraction as follows.

Total Water Content (TWC): TWC is the sum of the IWC and the LWC:

$$\mathrm{TWC}(t) = \mathrm{LWC}(t) + \mathrm{IWC}(t) \tag{6}$$

Supercooled liquid fraction (SLF): The SLF is a measure for the phase ratio (liquid to all), which is calculated using the LWC and IWC following Komurcu et al. (2014):

$$\mathrm{SLF}(t) = \frac{\mathrm{LWC}(t)}{\mathrm{LWC(t)} + \mathrm{IWC(t)}} \tag{7}$$

Consequently, the SLF ranges from 0 (pure ice cloud) to 1 (pure liquid cloud), with all values in between denoting mixed-phase clouds.

2.3 Auxiliary data

The fetch (distance from the sea ice edge) was calculated for each 5 s in-cloud measurement. This distance was determined using the 10 m wind field taken from MERRA-2 (Gelaro et al., 2017), and the sea ice concentration data from Nimbus-7 (Di-Girolamo et al., 2022) at the time of measurement. A total of 200 25-km-steps were performed upwind from the measurement location (downwind when measurement were above sea ice) until a sea ice concentration of >=20 % was reached. The final distance was then calculated as the number of steps taken to reach the sea ice edge, multiplied by the step distance of 25 km.

The mCAO index M index values were calculated using data from the fifth generation of ECMWF atmospheric reanalysis ERA5 (C3S, 2018). The sea ice edges found in Figures 1, and A3 to A11 are regridded values of the 25 % level of sea ice concentration calculated from AMSR2 data using the ARTIST sea ice algorithm (ASI 5, Spreen et al., 2008).

https://doi.org/10.5194/egusphere-2026-1650
Preprint. Discussion started: 16 April 2026

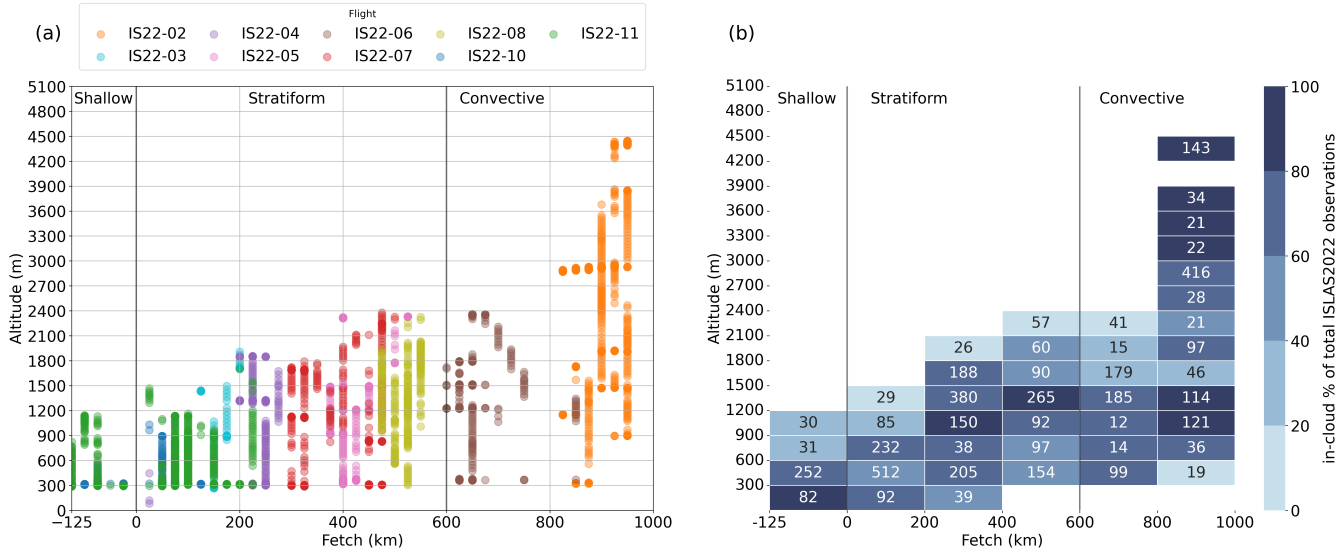

Figure 4. (a) The distribution of single 5 s in-cloud observations with respect to altitude and fetch, color-coded by ISLAS2022 flight numbers. (b) Number of 5s in-cloud observations per altitude-fetch bin and the corresponding in-cloud percentage (color-coded). Both plots cover the "Shallow", "Stratiform", and "Convective" regimes.

2.4 Data filtering

The analysis is focusing on mCAO clouds over sea ice and open ocean within the mixed-phase temperature range (0 to -35°C). A measurement is defined as in-cloud if either or both the LWC and IWC were above 0.01 $\mathrm{g\,m^{-3}}$ following Korolev and Milbrandt (2022). The flight paths included straight leg runs, saw tooth patterns, spirals, and step laddering through the cloud decks. Measurements during sharp turns, where the aircraft's roll exceeded ± 5 degrees, and where the change in heading exceeded ± 1 degree, have been removed from the analysis to limit flow-induced errors from the largest changes in airflow (Spanu et al., 2020). Further, the measurements where the fetch edge exceeded 1000 km were removed from the analysis due to the low number of observations that only covered a limited area at cloud top.

2.5 Composite approach

A dataset that covers all parts of the mCAO development is needed to investigate how the cloud microphysical properties evolve as the fetch increases. When plotting each of the 5 s in-cloud observations against the calculated fetch and altitude (see Figure 4 a), it becomes evident that each of our selected flights from the ISLAS2022 flight campaign only offers snapshots into certain parts of the mCAO evolution. Hence, a composite approach was developed that integrates the in situ microphysical observations from all flights throughout the campaign in order to capture the entire mCAO development from the sea ice to the Norwegian Coast.

https://doi.org/10.5194/egusphere-2026-1650
Preprint. Discussion started: 16 April 2026

When using the full dataset as a composite, it covers several days and therefore also necessarily variations in the meteorological situation. As this study is interested in the general development of the mCAO clouds and not detailed features relating to single flights, statistics were calculated at discrete fetch (horizontal dimension) and altitude (vertical dimension) intervals. The sizes of the altitude and fetch bins used in this composite analysis were chosen as follows:

Altitude binning: Altitude measurements are divided into 300 m bins from the surface up to the highest observed altitude. This altitude bin size was selected to ensure a sufficiently large amount of observations in each bin.

Fetch binning: The fetch was divided into 200 km bins. This bin size was chosen to ensure a relatively equal number of observations per fetch bin to keep the statistics comparable. The longest distance over sea ice was 125 km from the sea ice edge, so the first fetch bin covers only -125 to 0 km.

Any altitude-fetch combination that had less than 10 in-cloud observations has been removed from the analysis to ensure sufficient sample sizes. This results in the number of measurements per altitude-fetch bin to range from 12 to 512, with a mean of 58 measurements (see Figure 4b).

3 Results

In this section evolution of the composite mCAO clouds is shown for the selected ISLAS2022 flights. To begin, a couple of regions are defined at similar development stages within the mCAO evolution to make the overall analysis easier to follow. Subsequently is shown how the observations distribute over the altitude-fetch composite and how the TWC changes over the mCAO evolution. Next, the in-cloud temperature is investigated in the dataset and how the SLF changes through the mCAO composite. Finally, differences in the evolution of the liquid water and ice crystal parameters are discussed.

3.1 Regions of the mCAO evolution

The cloud observations are grouped into three regions, as illustrated in Table 2. This grouping is based on observed shifts in the microphysical properties during cloud evolution at specific distance points when using the composite described in Sect. 2.5. The first shift occurs at the sea ice edge, where the clouds change from the shallow clouds observed over sea ice and the mCAO development after the air mass reached the open ocean. This region is called the "Shallow" region, and this is the only region over sea ice. The second shift occurs around the 600 km mark, with clouds closer to the sea ice edge having more liquid at the cloud top, while clouds beyond the 600 km point are more and more glaciated.

This glaciation is often observed as the clouds become more convective, with increasing vertical motions and turbulence that keeps the ice crystals longer aloft and available for secondary ice production (Karalis et al., 2022). Overall, this led to three distinct regions in the mCAO development analysis, summarized in Table 2.

The general composite characteristics in the cloud observations show a development of the mCAO clouds which is consistent with the current understanding of mCAO cloud evolution found in other literature, where clouds are observed that develop and deepen as they move away from the sea ice edge (Brümmer, 1996; Fletcher et al., 2016; Dahlke et al., 2022). More liquid is observed at the cloud tops for the "Stratiform" region while clouds are generally more glaciated and uniform in the vertical

https://doi.org/10.5194/egusphere-2026-1650
Preprint. Discussion started: 16 April 2026

Table 2. Summary of composite region main features.

Region	I	II	III
Surface type	Sea ice	Ocean	Ocean
Fetch	-125 km - 0 km	0 km - 600 km	600 km - 1000 km
Cloud type	Shallow	Stratiform	Convective
Cloud development stage	Shallow, undeveloped	Shallow, developing	Deep, maturing
Cloud top phase	Ice	Liquid	Increasingly glaciated

extent for the "Convective" region. This consistency with other studies supports the view that the composite approach employed here is robust.

3.2 Distribution of observations

Figure 4b shows the distribution of the 5 s observations per altitude-fetch bin within the composite dataset. The sum of in-cloud observations from all altitude bins per fetch bin is fairly equal, with approximately 1000 observations per 200 km bin. The exceptions are the "Shallow" region, which has less than 400 observations, and the first fetch bin of the "Convective" region, which has less than 600 observations. The selected in-cloud observations also cover a decent amount of the total number of observations in the composite altitude-fetch bins. As can be seen from the percentage of in-cloud observations, as shown by the colorbar in Figure 4b), 40 % or more of the total observations are included in the in-cloud dataset. Only a few bins have a smaller percentage, mostly located at cloud top.

The mCAO cloud development is also evident in this distribution of the composite dataset. The cloud height increases gradually through the "Stratiform" region from the initial height in the "Shallow" region, as the air moves across the warmer sea surface. The deepest and most mature clouds are found at the greatest fetch in the "Convective" region, with cloud tops reaching up to 4500 m. The large step in cloud height in the "Convective" region is likely exaggerated due to the single flight that has a significantly different main wind direction from the other flights, see Figure 4 a.

3.3 Composite development of TWC and SLF

The mean TWCs for each of the altitude-fetch bins are shown in Figure 5a. TWC is very low in the "Shallow" region over the sea ice (0.04 to 0.11 $\mathrm{g\,m^{-3}}$), with the highest TWC values found near the cloud base. This changes in the "Stratiform" region where the air mass experiences increased heat and moisture fluxes over the open ocean, resulting in a gradual increase in the TWC, reaching values up to 0.31 $\mathrm{g\,m^{-3}}$. There is an abrupt increase in the TWC values as the clouds reach the "Convective" region. The highest amounts of cloud water can be found here, and the TWC values are large throughout the cloud (mostly 0.22-0.37 $\mathrm{g\,m^{-3}}$). This abrupt increase is likely linked to a shift to more convective clouds. As will be shown later, the increase in TWC is linked to a rapid increase in IWC, resulting from both an increased amount and size of ice crystals, while the LWC becomes lower. This indicates that the crystals remain aloft longer before sedimenting out of the cloud as a result of stronger

https://doi.org/10.5194/egusphere-2026-1650
Preprint. Discussion started: 16 April 2026

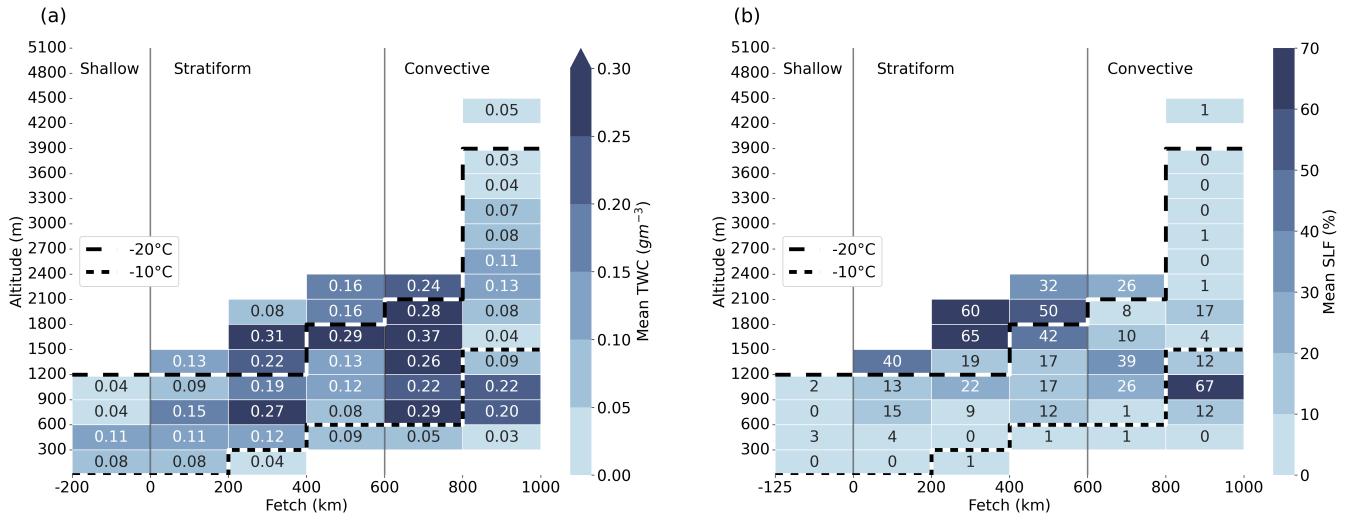

Figure 5. (a) Mean TWC per altitude-fetch bin (color-coded and indicated by mean TWC value). (b) Mean SLF for the in-cloud observations per altitude-fetch bin. Both plots show the borders between the composite regions; "Shallow", "Stratiform" and "Convective". Dashed lines indicate where the mean temperature of the altitude-fetch bins shifts to below -20°C (long dashes) and to below -10°C (short dashes)

updrafts, allowing them to grow at the expense of the droplets. At the end of the "Convective" region, much lower TWC values are observed. These are the deepest clouds but their TWC has fallen to values that resemble the values observed close to the sea ice edge for most of the altitude bins (below $0.13\,\mathrm{g\,m^{-3}}$ at altitudes above $1200\,\mathrm{m}$). These low TWC values are likely attributable to increased entrainment of dry air in the vertically developed clouds, as well as efficient precipitation formation through the ice phase. These clouds are more aged clouds, as will be discussed further when looking at the complementary cloud parameters.

Another observation is that TWC has low values at the lowest altitude bins at all distances. Later, it will be shown that the SLF values in these bins are close to zero, indicating that most of the observed particles are ice. These low values at the cloud base altitudes are likely due to measurements made in precipitation directly below the clouds, as we would expect the precipitation to consist of mostly larger ice particles. The precipitation particles will in most cases exceed the instrument detection limit (>$1600\,\mu\mathrm{m}$), which leads to an underestimated TWC in precipitating clouds. This is also supported by CIP images showing larger ice crystals, truncated at one or both sides of the photodiode array. Despite the "all-in" sample volume correction, mass beyond $1600\,\mu\mathrm{m}$ particles is completely lost.

Figure A1 shows the composite temperature evolution for the in-cloud values. To more easily identify the altitude-fetch bins with mean temperature below -20 °C and -10 °C, dashed lines indicating these isotherms have been added to Figures 5 and 6. The "Shallow" region shows no significant variation in mean temperature between the different altitude bins (cloud top at -14 °C), consistent with the rather stable temperature conditions expected over sea ice. The temperature at a given altitude bin increases with increasing fetch as the mCAO clouds are subjected to the warmer ocean surface. The warmest clouds are

https://doi.org/10.5194/egusphere-2026-1650
Preprint. Discussion started: 16 April 2026

naturally found in the "Convective" region at the largest fetch, where above -20 °C can be found up to almost 4000 m altitude. In parallel to this increase in temperature with fetch, cloud top cooling is observed as the clouds deepen into higher and colder altitudes. The coldest cloud tops are found in the "Stratiform" region (-23 to -28 °C).

When examining how the TWC from Figure 5a is divided by phase, as shown by the SLF in Figure 5b, low SLF values are found in the "Shallow" region (<3 %). Consequently, the condensed water content of clouds over sea ice was dominated by ice for our observations. The SLF increases in the "Stratiform" region with liquid water becoming dominant at and near cloud top (up to 65 %). In the "Convective" region, the clouds continue to glaciate and are dominated by ice except for in a single altitude-fetch bin near cloud base.

To understand what causes the observed changes in the SLF with fetch, in the following the composite evolution of the liquid water droplet and ice crystal features are considered separately.

3.4 Cloud liquid properties

The composite values of the cloud liquid properties (CDNC, ED and LWC) can be found in Fig. 6a, c, e. The overall composite cloud droplet mean ED was 16 µm, which is consistent with a couple of other studies; Young et al. (2016) observed effective diameters over sea ice ranging from 8 µm to 24 µm. Comparably, Klingebiel et al. (2023) measured effective diameters in a similar range as Young et al. (2016) but with a maximum at 14 µm. Overall, this study did not observe much liquid in the "Shallow" region with negligible LWCs and CDNC for most of the cloud altitude bins. This also means that the mean ED values in the "Shallow" region are not representative values, as it is likely they result from only a handful of particles detected by the CDP. The samples used in the "Stratiform" region bins are still considered in-cloud since our selection criteria of IWC or LWC greater than 0.01 $\mathrm{g\,m^{-3}}$ allows for the LWC to be below this threshold if the IWC is above, that is, the cloud consist purely of ice. This is also true for the bins in the two other regions where the CDNC is close to zero, the cloud liquid property values for these bins are therefore hatched in Fig. 6.

For the "Stratiform" region, an increase in CDNC is observed, especially close to cloud top, where the largest bin mean concentrations are found (CDNC > 40 $\mathrm{cm^{-3}}$). A similar vertical profile of the CDNC has been observed by (Järvinen et al., 2023) during the ACLOUD campaign conducted in May-June 2017. However, in contrast, other studies such as Mioche et al. (2017) show a decrease in CDNC towards the cloud top. The ED in the "Stratiform" region begins as a smaller-than-average ED in the area closest to the sea ice, where the highest CDNC ar also found close to cloud top. However, with increasing fetch, the CDNC gradually decreases and the droplet ED increases and exceeds the composite mean by more than 5 µm.

The LWC stays low at cloud base in the "Stratiform" region, but increases towards cloud top as the cloud droplet ED increases. This is consistent with an adiabatic LWC profile (see Fig. 6a). The region within the cloud that shows higher LWC deepens with increasing fetch, with a maximum LWC of 0.23 $\mathrm{g\,m^{-3}}$. This increase in liquid at cloud top and deepening of the clouds with increasing fetch is well-documented for mCAO clouds (Murray-Watson et al., 2023; Ruiz-Donoso et al., 2020; Schirmacher et al., 2024; Young et al., 2016; Aragon et al., 2025; Karalis et al., 2022), and is consistent with the developing stratocumulus street region of the mCAO. The LWC drops to lower values again in the "Convective" region, with a few

https://doi.org/10.5194/egusphere-2026-1650
Preprint. Discussion started: 16 April 2026

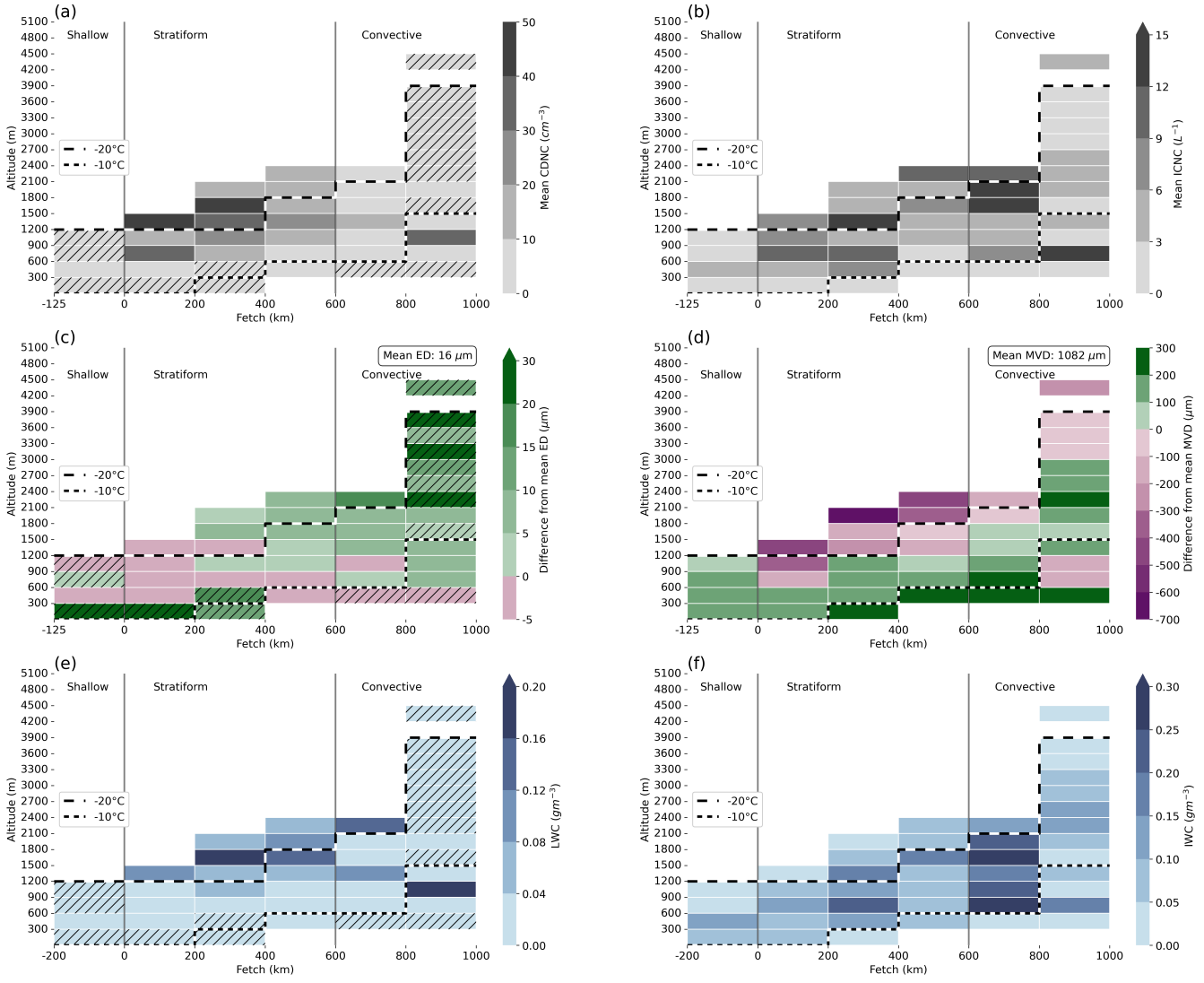

Figure 6. Distribution of in-cloud liquid droplet (CDP) and ice crystal (CIP) properties per 300 m altitude and 125 km fetch bins. a) Mean cloud droplet number concentration (CDNC), b) Mean ice crystal number concentration (ICNC), c) Difference from the mean effective diameter (ED). d) Mean crystal volume diameter (MVD), e) Mean LWC, f) Mean IWC. All CDP values are calculated for particles larger than 6 μm and all CIP values are calculated for particles larger than 100 μm. All plots show the borders between the composite regions; "Shallow", "Stratiform" and "Convective". Dashed lines indicate where the mean temperature of the altitude-fetch bins shifts to below -20 °C (long dashes) and to below -10 °C (short dashes). Hatched bins in panels a, c, and e indicate bins with negligible observede liquid water content.

exceptions: remnant layers of bin mean LWC above 0.08 $g\,m^{-3}$ for the cloud top, and a bin mean LWC above 0.16 $g\,m^{-3}$ towards the cloud base. The latter is collocated with some of the higher temperatures >-10 °C (see Fig. A1).

https://doi.org/10.5194/egusphere-2026-1650
Preprint. Discussion started: 16 April 2026

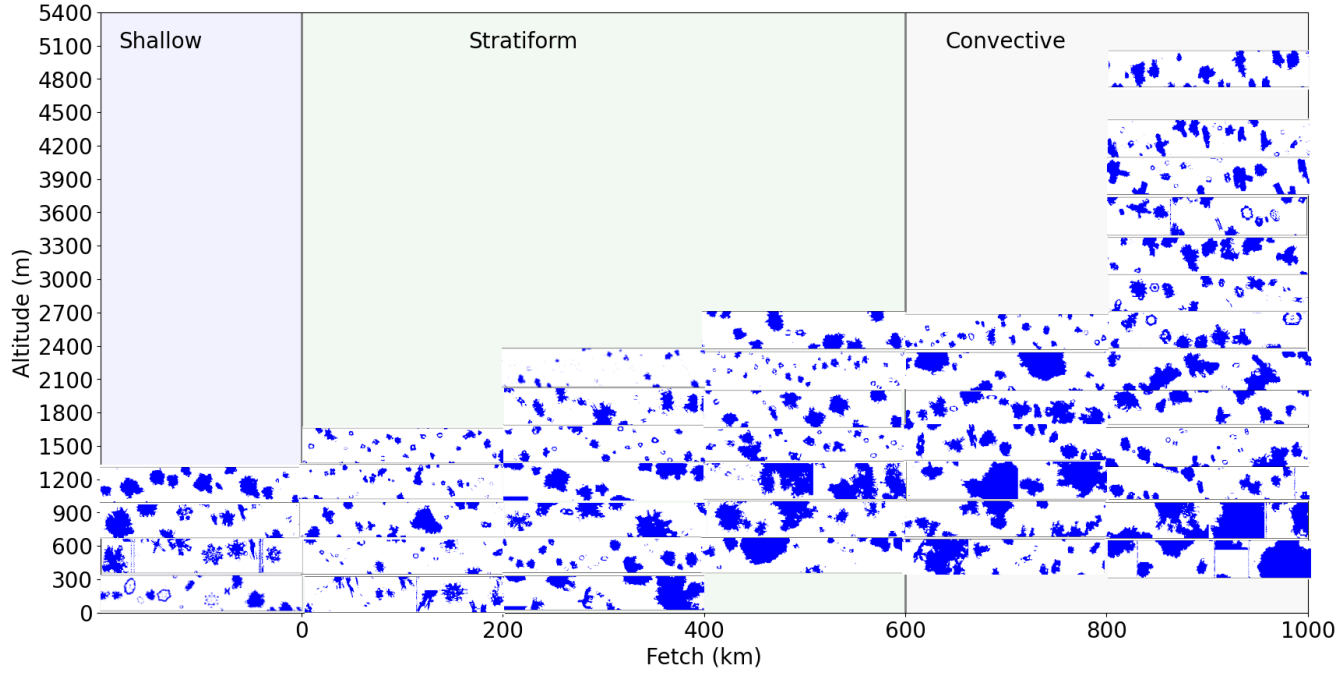

Figure 7. Selection of CIP images for the composite dataset. Each altitude-fetch bin contains an exemplary snapshot of particles imaged by the CIP. The snapshots were chosen either because they were close to the middle of a larger set of consecutive measurements in the same altitude-fetch bin (for bins with more than 50 in-cloud measurements), or as a representative sample from that altitude-fetch bin (for bins with less than 50 in-cloud measurements).

The clouds become primarily glaciated in the "Convective" region (SLF less than 40 % for nearly all altitude-fetch bins), and nearly all the altitude-fetch bins have a CDNC below 10 cm^{-3}. The few droplets that remain are generally larger than the composite mean by more than 20 µm near the center of the clouds, albeit with limited statistics. This is consistent with only the largest cloud droplets surviving sub-saturated conditions as would be expected in glaciating clouds and when the WBF process is ongoing (Korolev, 2007). This is also where updrafts are expected to be maximized in vertically developed clouds, which means that vertical velocities may locally be large enough to sustain both ice crystal and cloud droplet growth.

3.5 Cloud ice properties

The composite values of the cloud ice properties (ICNC, MVD and IWC) can be found in Figure 6b, d, f. Additionally, the ice crystal images from the CIP is shown in Fig. 7. The "Shallow" region has low ICNC values, the maximum is towards cloud base with the maximum bin mean value of 3 L^{-1}, and the largest mean MVD for the "Shallow" region is 1244 µm. The overall composite mean MVD value was 1082 µm, and for the "Shallow" region all altitude layers show larger values than this mean, and the MVD value stays fairly equal throughout the cloud. From the ice crystal images in Fig. 7 we also observe that the ice

https://doi.org/10.5194/egusphere-2026-1650
Preprint. Discussion started: 16 April 2026

crystals in this region to a large degree are pristine ice crystals. The pristine habits were dendritic or plate-like, consistent with the observed temperature over sea ice of -12 to -14 °C (Hueholt et al., 2022).

Ice dominates the clouds in the "Shallow" region, which has been observed when comparing the SLF values in Fig. 5b and TWC values in Fig. 5a, although the values of ICNC and IWC are in the lower end of the composite range. While some studies have found that Arctic low-level clouds in spring are more likely mixed-phase or liquid-dominated (Moser et al., 2023; Young et al., 2016), others have found ice-dominated MPCs over sea ice Klingebiel et al. (2023). In our case, the cloud top temperatures were warmer over sea ice than over ocean (around -14 °C, see Fig. A1). This points to a possible explanation for the occurrence of ice clouds being linked to local sources of INPs (e.g., marine biological particles) due to areas of liquid water within the ice, such as open leads (Dall´Osto et al., 2017; Bigg and Leck, 2001). Since pristine ice crystals are observed in these clouds, other possible explanations such as blowing snow (e.g., Hofer et al., 2021; Papakonstantinou-Presvelou et al., 2022) are less likely.

Furthermore, in the "Stratiform" region in Figure 6, panel (b) shows an increase in ICNC through most of the cloud, except at cloud base where the ICNC remains low. Cloud base is also where the lowest (close to zero) values of ICNC are found; however, the ICNC values here are likely affected by the largest particles being excluded due to the sizing limitations of the CIP. The largest mean MVD at cloud base in the "Stratiform" region is 1433 μm. Beside these low values at cloud base, the ICNC in the "Stratiform" region varies from 3 L^{-1} to 15 L^{-1} throughout the cloud.

The vertical distribution of IWC in the "Stratiform" region is relatively uniform in the vertical extent, with most altitude bins having a bin mean IWC between 0.05 $\mathrm{g\,m}^{-3}$ and 0.20 $\mathrm{g\,m}^{-3}$. In addition, the lowest values can be found at cloud top (see Fig. 6f), which prevents cloud droplet evaporation through the WBF process and contributes to the higher amounts of liquid water in this area together with the possible entrainment of CCNs from the air above. In contrast, the WBF should be active further down in the cloud where cloud ice is abundant, and thus cause cloud droplets to evaporate, consistent with the observed smaller ED. The strongest gradient in MVDs from cloud top to base is observed in the "Stratiform" region with some of the highest bin mean MVDs found at the cloud base furthest from the sea ice edge. It should be noted that a bin MVD anomaly of 300 μm suggests that several particles have been close to or exceeded the CIP detection limit of 1600 μm, indicating that larger snow particles were likely undetected. A MVD close to the CIP detection limit at the lowest altitude bin, especially combined with little to no liquid water (low ED and CDNC) is a strong indication that the measurements from this altitude bin are likely dominated by precipitation in the form of snow, and that the actual cloud base is closer to the next altitude bin. This affects the calculated IWC in addition to the ICNC due to particles exceeding the CIP size threshold, as mentioned above. This is especially observed for the last fetch bin of the "Stratiform" region and all of the "Convective" region, and Fig. 7 shows multiple ice crystals that would have been excluded by the "all-in" correction described in Sect. 2.2.2 in these altitude-fetch bins. The vertical structure of smaller ice crystals towards the top of the cloud and larger ice crystals towards the base of the cloud is very pronounced in the "Convective" region. In this region, the smallest particles at the top of the cloud are up to 600 μm larger than the smallest particles at cloud top for the "Stratiform" region. This indicates that larger particles generally reach higher levels in the "Convective" region, due to the stronger updrafts associated with the deeper convection. At cloud base of the deepest cloud layer at the end of the "Convective" region two altitude bins are observed with MVD slightly lower

https://doi.org/10.5194/egusphere-2026-1650
Preprint. Discussion started: 16 April 2026

than the composite mean. This does not include the lowest altitude bin, which is likely a precipitation layer, with MVD close to the CIP upper detection limit. The two areas with lower MVD coincides with the altitude bin with significantly higher CDNC than for the rest of the cloud at this distance, which could be due to the limited statistics we have for this area.

The ICNC in the "Convective" region is in the higher range (>6 L^{-1}) for most of the bins in the fetch bin closest to the sea ice edge. Also, a strong increase in IWC is observed at all altitudes following the transition from the "Stratiform" to "Convective" region, with the largest bin mean IWC of 0.35 $\mathrm{g\,m}^{-3}$. However, these high IWC values do not persist across the entire "Convective" region. In the deepest clouds, furthest from the sea ice, ICNC values are found in the lower range (<6 L^{-1}), and the mean bin IWC reach 0.17 $\mathrm{g\,m}^{-3}$.

The shift toward a more glaciated state that is observed between the "Stratiform" and the "Convective" region is a typical feature found in mCAO clouds after the clouds have transitioned into a cellular structure (Murray-Watson and Gryspeerdt, 2024; Mages et al., 2023; Abel et al., 2017; Lloyd et al., 2018). The transition from the stratocumulus streets to the more cellular cloud structure is also often linked to a change in cloud base altitude. In the underlying dataset, the lowest in-cloud altitudes vary between 83 - 289 m for observations in the "Stratiform" region and between 301 - 355 m for observations in the "Convective" region. This lifting and deepening of the cloud in combination with a drop in CDNC at the cloud top after the transition is consistent with the observations of Young et al. (2016).

However, it should be noted here that the different behaviors between the two parts of the "Convective" region may be influenced by the fact that this region contains data from only two flights, limiting the statistics.

4 Discussion

The presented results show high amounts of ice, and IWC generally dominates the TWC. Several other studies, such as Abel et al. (2017) and Young et al. (2016), show far higher amounts of liquid, especially during the initial cloud development stage closest to the sea ice edge. Abel et al. (2017) measured LWC close to TWC for the stratiform region, with values up to 0.7 $\mathrm{g\,m}^{-3}$, while the "Ocean" profiles from Young et al. (2016), which is a study that most closely compares to the "Stratiform" region of this study, showed LWC values up to 0.5 $\mathrm{g\,m}^{-3}$. This is far higher than the highest bin mean LWC of 0.2 $\mathrm{g\,m}^{-3}$ from our "Stratiform" region. Although the amount of liquid from Young et al. (2016) is higher than observed during ISLAS2022, their highest LWC values are found towards top of the cloud, just as is the case for the "Stratiform" region of this ISLAS2022 dataset. The size of the liquid droplets in Young et al. (2016) also compare well to ISLAS2022 observations. Their effective diameter ranges from 8 µm at cloud base to 22 µm at cloud top, compared to the observed EDs of 10 µm to 26 µm from this study.

The difference in ice amounts observed during ISlAS2022 compared to Abel et al. (2017) and Young et al. (2016) could be connected to differences in the in-cloud temperatures. While the lowest temperatures observed in Young et al. (2016) are slightly below -20 °and in Abel et al. (2017) are about -15°C, the ISLAS2022 dataset spans in-cloud temperatures down to -28 °C.

https://doi.org/10.5194/egusphere-2026-1650
Preprint. Discussion started: 16 April 2026

Some of the largest ice crystals measured are found in the "Convective" region, as seen in Fig. 7. While the largest ice crystals in this region were measured close to cloud base, large rimed and aggregated crystals were also found almost up to 2500 m altitude. Pristine ice crystals, including bullet rosettes, are reappearing at the upper half of the deepest clouds in the "Convective" region. The liquid water must therefore be close to depleted for altitudes with pristine crystals, excluding growth by riming as a possible ice crystal growth process. This is also confirmed by the very low LWC values observed in this area (Fig. 6e).

Overall, the composite analysis of this study allows to follow more of the evolution of mCAO clouds for the ISLAS2022 dataset, compared to the limited portion an individual flight would cover. The composite evolution is consistent with previous literature and the current understanding of underlying microphysical processes. While this demonstrates that such a composite analysis can serve as a powerful method to gain additional insight by combining data from individual research flights, some caveats to the present study must be admitted. Notably, as previously mentioned, the "Shallow" and the "Convective" regions are composites based on the observations from only two flights each. More specifically, IS22-10 and IS22-11 cover the "Shallow" region (both from the same day), while IS22-02 and IS22-06 cover the "Convective" region. The limit in available flight data is perhaps most visible in the "Convective" case, where the cloud evolution within the region is rather abrupt. The "Convective" region is covered by two flights, IS22-06 and IS22-02, the latter being a flight with a westerly main wind direction, in opposition to the largely northerly main wind direction during the other flights (see Figures A3-A11). This low number of flights and the limited overlap between these two flights may affect the robustness of the reported findings in this region. The composite evaluation is naturally more susceptible to bias when the number of flights covering an area is low. When there are more flights covering a region, as for the "Stratiform" region, we observed a smoother evolution of the clouds through the region.

5 Conclusions

This study presents a composite approach to airborne in situ observations to study the evolution of the microphysical properties of mCAO clouds encountered during the ISLAS2022 campaign. For this purpose, the measured (cloud droplet and ice crystal number concentration, effective diameters) and derived (liquid and ice water content, supercooled liquid fraction) microphysical properties with respect to their altitude and distance to the sea ice edge (fetch) have been investigated.

Overall, the observed mCAO structure compares in most aspects to what other studies that focus on individual flights and case studies have found. Based on micro- and macrophysical properties of the clouds, three development stages have been considered: (a) a "Shallow" region describing thin, low ice clouds over the sea ice, (b) a "Stratiform" region encompassing closed and open mesoscale cellular convection that evolves with increasing fetch, and (c) a "Convective" region showing deep, glaciated clouds that reach the end of their lifetime.

The strength of the composite approach in the "Shallow" region becomes evident when looking at the mCAO cloud as a whole, and the differences between this shallow region and the other two regions. Once over open ocean ("Stratiform" region), the clouds deepen as expected and new droplet formation is observed likely due to an increase in available moisture and CCNs from the open sea. In general, in the "Stratiform" region cloud droplet concentration and size increases with height and are

https://doi.org/10.5194/egusphere-2026-1650
Preprint. Discussion started: 16 April 2026

maximized near cloud top, which is at least true for altitudes above 300 m. The ice crystal formation is initiated near cloud top, as we find the smallest ice crystal sizes in this area. This is also where the lowest in-cloud temperatures are found (generally below -20 °C), which could potentially mean that the INPs available for these mCAOs needed temperatures as low as this to activate. The ice crystals quickly begin to sediment through the cloud as they grow in size, which is substantiated by the decrease in ICNC and increase in MVD towards cloud base. These large ice crystals are too heavy to be kept aloft by the updrafts, so they initiate precipitation at the base of the clouds.

The "Convective" region starts off with increased glaciation (and likely also precipitation), probably linked to a shift to a more cellular structure. The "Convective" region covers two fetch bins between 600 and 1000 km, with quite an abrupt change between those two fetch bins, especially regarding TWC. The deepest, most mature clouds in the "Convective" region consisted of mainly large ice crystals and had low TWC. This is consistent with the description of decaying mCAO clouds (Lackner et al., 2023, 2024), where the generation of water droplets or ice crystals is rather limited.

Overall, by integrating the in situ observations from different flights into a single composite, the evolution of the mCAO clouds could be investigated in this study. One has to keep in mind that a limitation to this approach is the possibility of bias due to too few observations per region. Still, the approach should be much more robust, as compared to single cloud case studies. The lack of statistics is perhaps most identifiable in the "Convective" region where only two flights contribute with observations, and each of the flights mainly cover one of the two fetch bins (Fig. 4a). Consequently, the observed abrupt changes in microphysical properties between the fetch bins in the "Convective" region is due to statistics as compared to the "Stratiform" region, which integrates over seven flights covering multiple fetch bins.

The strength of this composite approach can be improved even more when incorporating observations from multiple campaigns in the future, stretching different years, seasons, and areas of the Arctic. A larger amount of statistics would also allow for finer binning of the dataset, which would enable us to study processes such as mCAO cloud break-up in more detail.

The alternative to the composite approach is to make a case analysis per flight. This approach has its merits, especially when looking at detailed processes and specific features that can be covered by a single flight. The full extent of mCAO evolution on the other hand, is difficult to have fully covered in both the vertical and the horizontal with single flights. Comparing different case study flights at different stages of the evolution is possible, however the composite approach offer much better spatio temporal coverage with flights overlapping in the distance from sea ice, and observed at different altitudes. In addition, this composite approach could also be a useful tool to identify how specific factors and processes (e.g., air temperature, sea surface temperature, pre-mCAO airmass trajectories, etc.) trigger changes in the mCAO evolution, with possible focus on regions where glaciation or dissipation occur .

Appendix A: Supplementary figures

Figure A1 shows the composite overview of the mean temperature in each altitude fetch bin from the ISALS2022 Spring Campaign. These means are the basis for the dashed -20°C (long dashes) and -10°C (short dashes) lines used in the other composite plots.

https://doi.org/10.5194/egusphere-2026-1650
Preprint. Discussion started: 16 April 2026

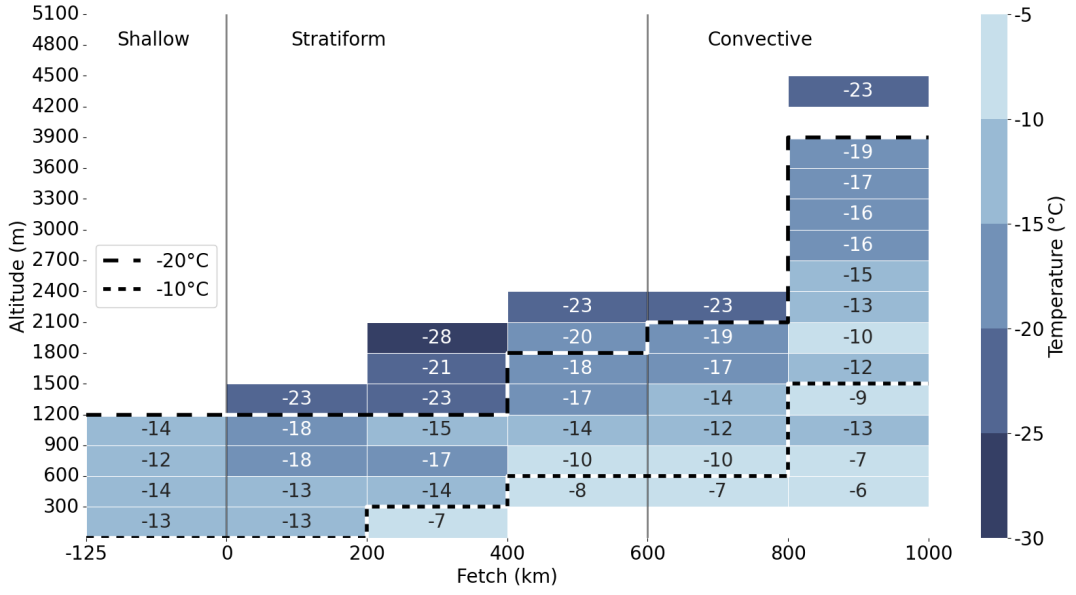

Figure A1. Mean temperature for the in-cloud observations per altitude-fetch bin. The borders between the composite regions; "Shallow", "Stratiform" and "Convective" are shown. Dashed lines indicate where the mean temperature of the altitude-fetch bins shifts to below -20°C (long dashes) and to below -10°C (short dashes)

https://doi.org/10.5194/egusphere-2026-1650
Preprint. Discussion started: 16 April 2026

Figure A2 shows examples of Lagrangian trajectories for the two flights that passed over sea ice (IS22-10 and IS22-11, both from 4 April 2022). The trajectories were calculated using the 10 m wind field from MERRA-2 (Gelaro et al., 2017), by stepping back in 30-minute intervals to visualize the air parcel's Lagrangian path before measurement. Sea ice concentration data came from from Nimbus-7 (DiGirolamo et al., 2022).

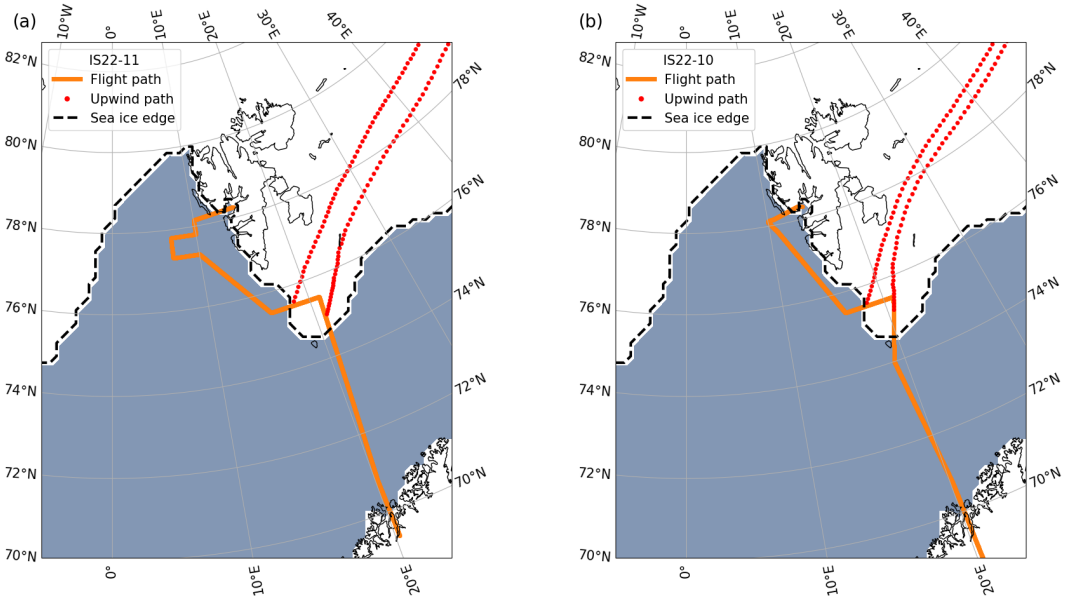

Figure A2. Trajectories for airmasses encountered during the flights over sea ice (IS22-10 and IS22-11).

https://doi.org/10.5194/egusphere-2026-1650
Preprint. Discussion started: 16 April 2026

Figures A3-A11 show overviews for each of the ISLAS2022 Spring campaign flights used in this study. In particular, panel a of each figure shows the flight path (in orange) on top of the closest collocated MODIS satellite image (MODIS Science Team, 2017) with the in-cloud measurements indicated as black dots. The windrose in the top left shows the wind directions encountered during the in-cloud observations. The wind direction is taken from meteorological measurements of the aircraft's navigational dataset. The sea ice edge of the day of the flight is shown as a red, dotted line (defined as the 25 % sea ice concentration boundary from ASMR2 - Advanced Microwave Scanning Radiometer for EOS - onboard the NASA satellite Aqua).

In panel b of each figure, the flight path is shown on top of the spatial distribution of the mCAO index calculated for this day (see Sect. 1 for details). The corresponding histogram of the mCAO indices encountered along the flight track is given in panel c of each figure.

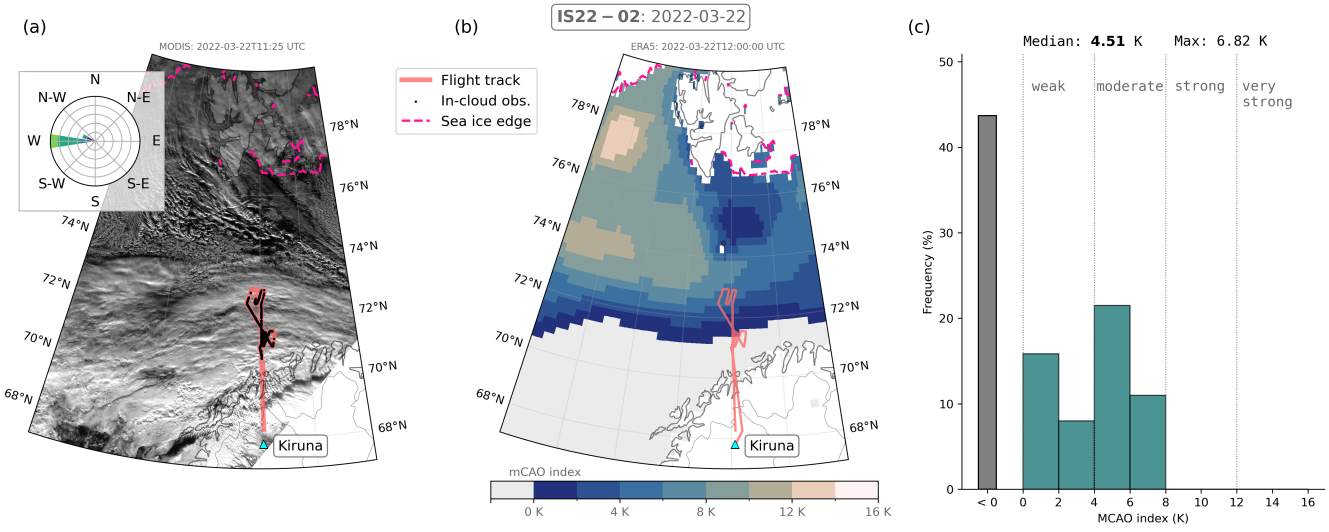

Figure A3. Flight and mCAO information from flight IS22-02. (a) Flight path, MODIS satellite image (Band 1: 620-670 nm wavelenght band), sea ice edge and wind direction. (b) Spatial distribution of mCAO index on day of flight. (c) Histogram of mCAO values along flight track.

https://doi.org/10.5194/egusphere-2026-1650
Preprint. Discussion started: 16 April 2026

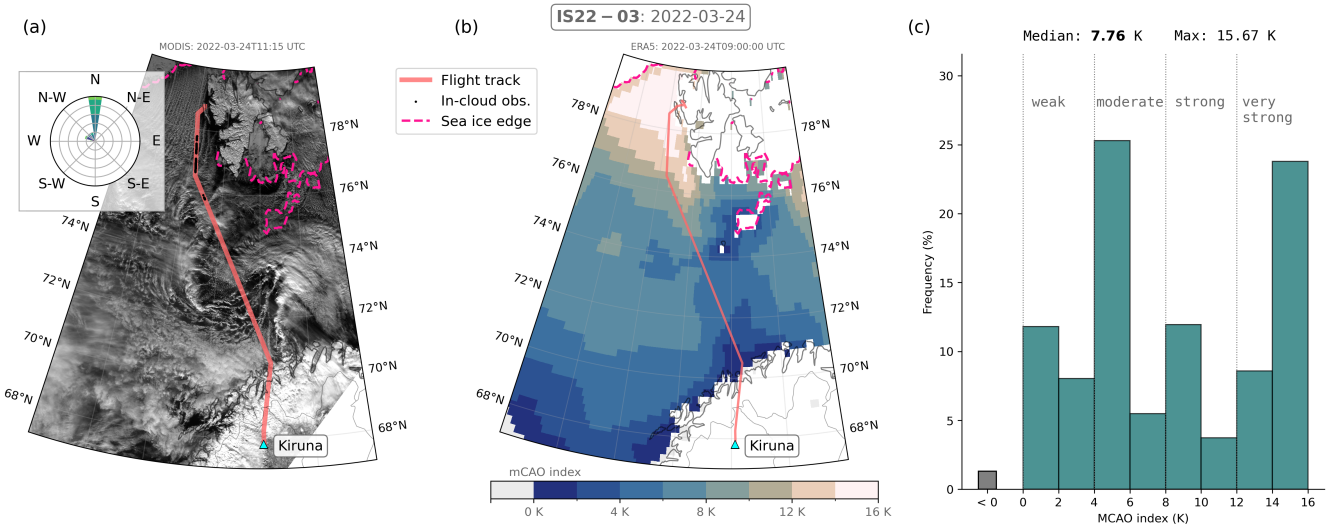

Figure A4. Flight and mCAO information from flight IS22-03. (a) Flight path, MODIS satellite image (Band 1: 620-670 nm wavelenght band), sea ice edge and wind direction. (b) Spatial distribution of mCAO index on day of flight. (c) Histogram of mCAO values along flight track.

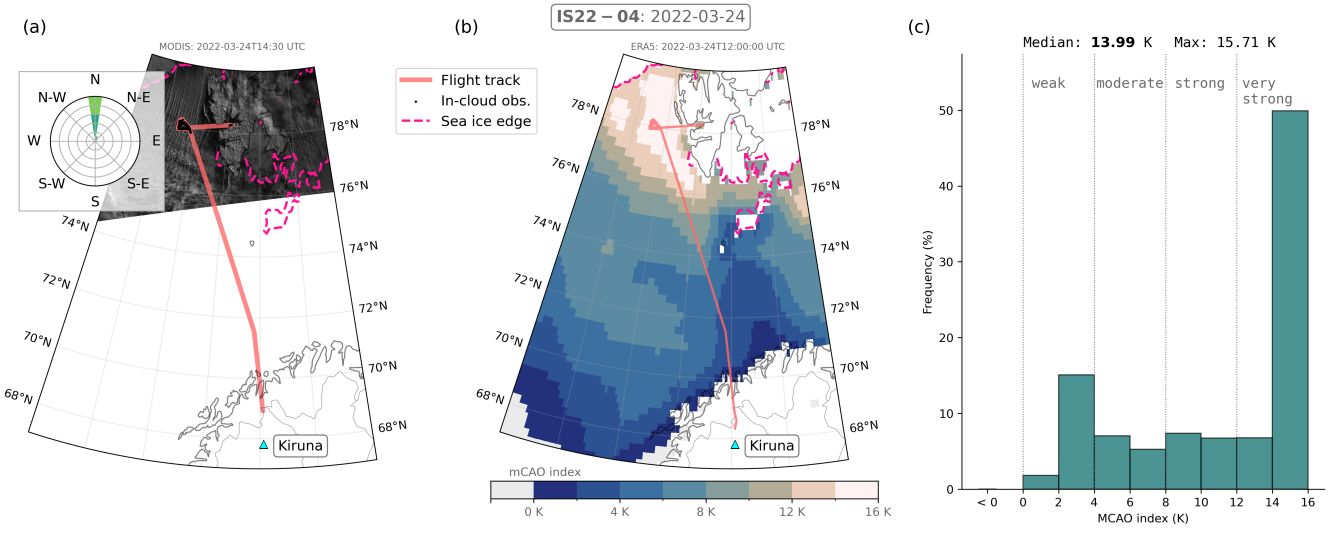

Figure A5. Flight and mCAO information from flight IS22-04. (a) Flight path, MODIS satellite image (Band 1: 620-670 nm wavelenght band), sea ice edge and wind direction. (b) Spatial distribution of mCAO index on day of flight. (c) Histogram of mCAO values along flight track.

https://doi.org/10.5194/egusphere-2026-1650
Preprint. Discussion started: 16 April 2026

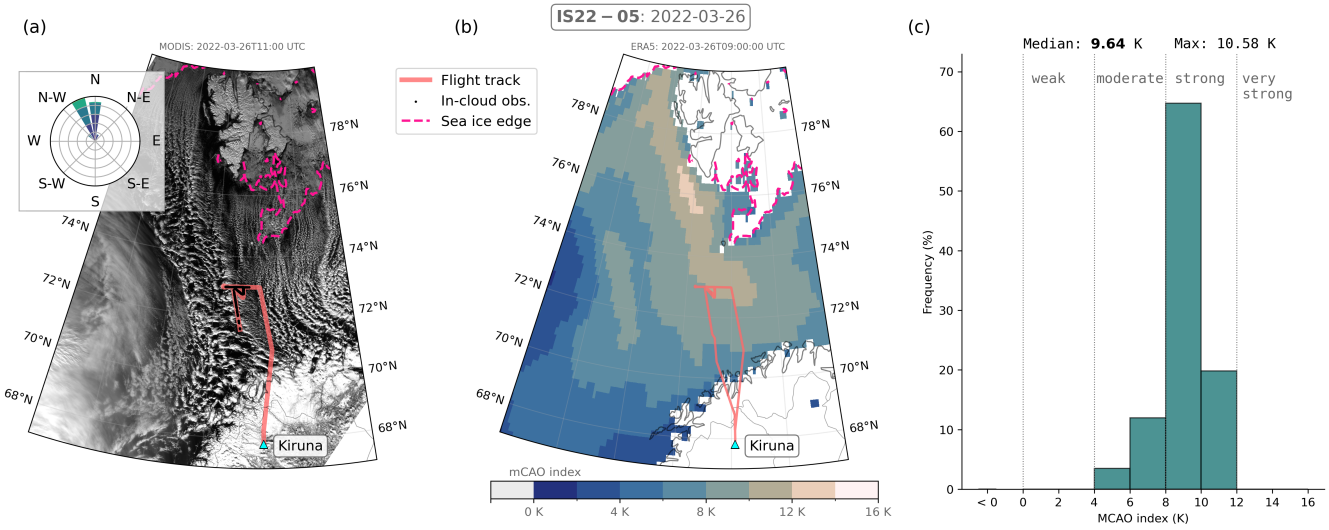

Figure A6. Flight and mCAO information from flight IS22-05. (a) Flight path, MODIS satellite image (Band 1: 620-670 nm wavelenght band), sea ice edge and wind direction. (b) Spatial distribution of mCAO index on day of flight. (c) Histogram of mCAO values along flight track.

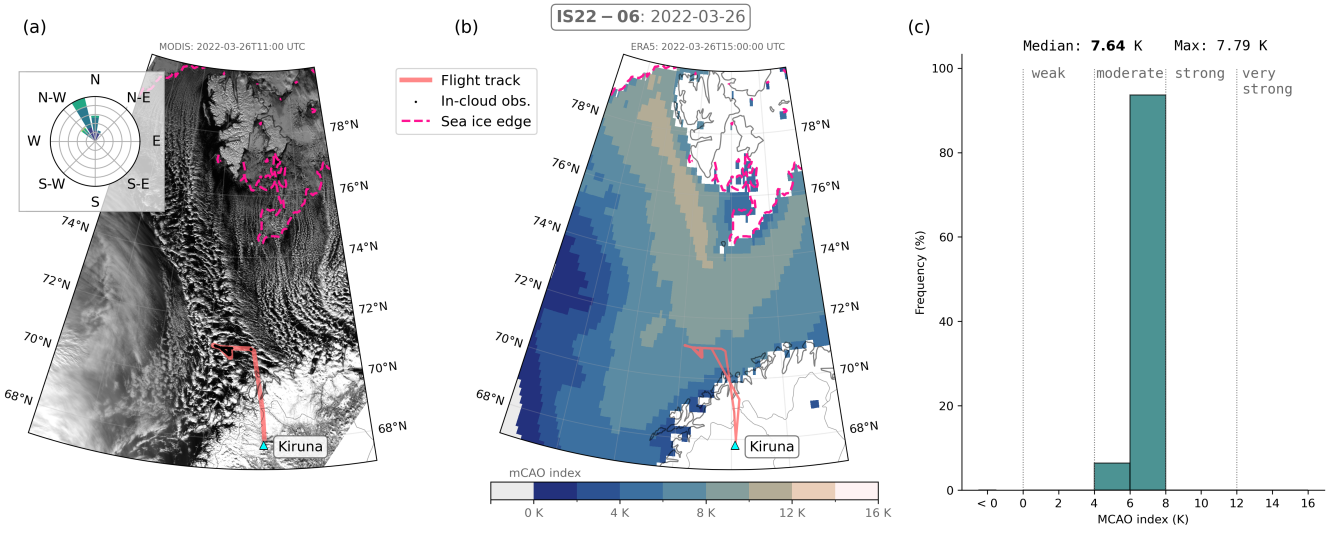

Figure A7. Flight and mCAO information from flight IS22-06. (a) Flight path, MODIS satellite image (Band 1: 620-670 nm wavelenght band), sea ice edge and wind direction. (b) Spatial distribution of mCAO index on day of flight. (c) Histogram of mCAO values along flight track.

https://doi.org/10.5194/egusphere-2026-1650
Preprint. Discussion started: 16 April 2026

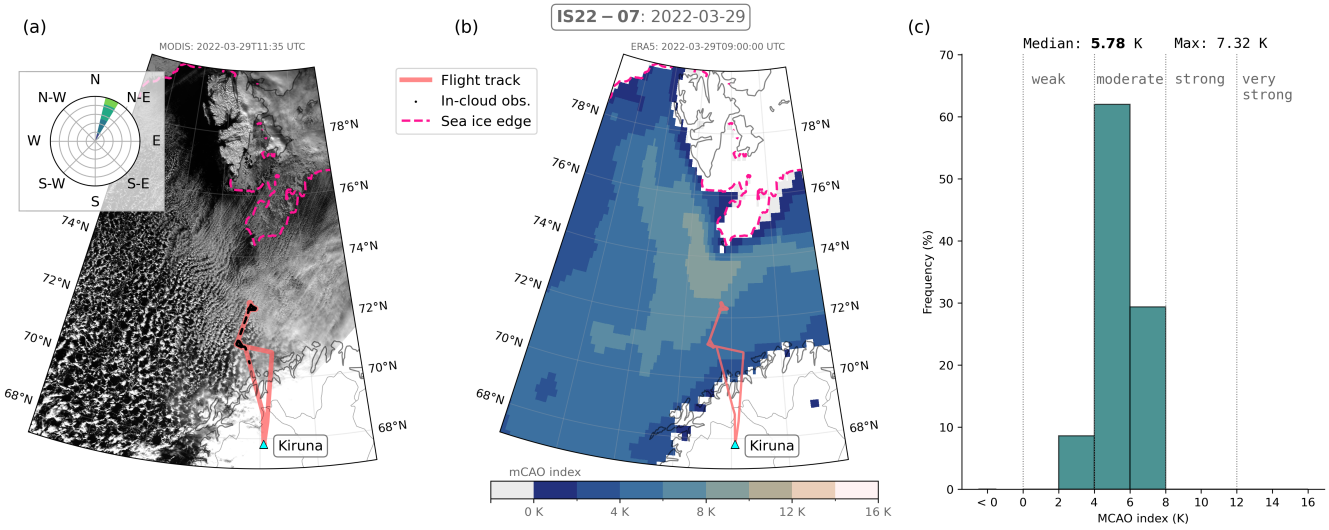

Figure A8. Flight and mCAO information from flight IS22-07. (a) Flight path, MODIS satellite image (Band 1: 620-670 nm wavelenght band), sea ice edge and wind direction. (b) Spatial distribution of mCAO index on day of flight. (c) Histogram of mCAO values along flight track.

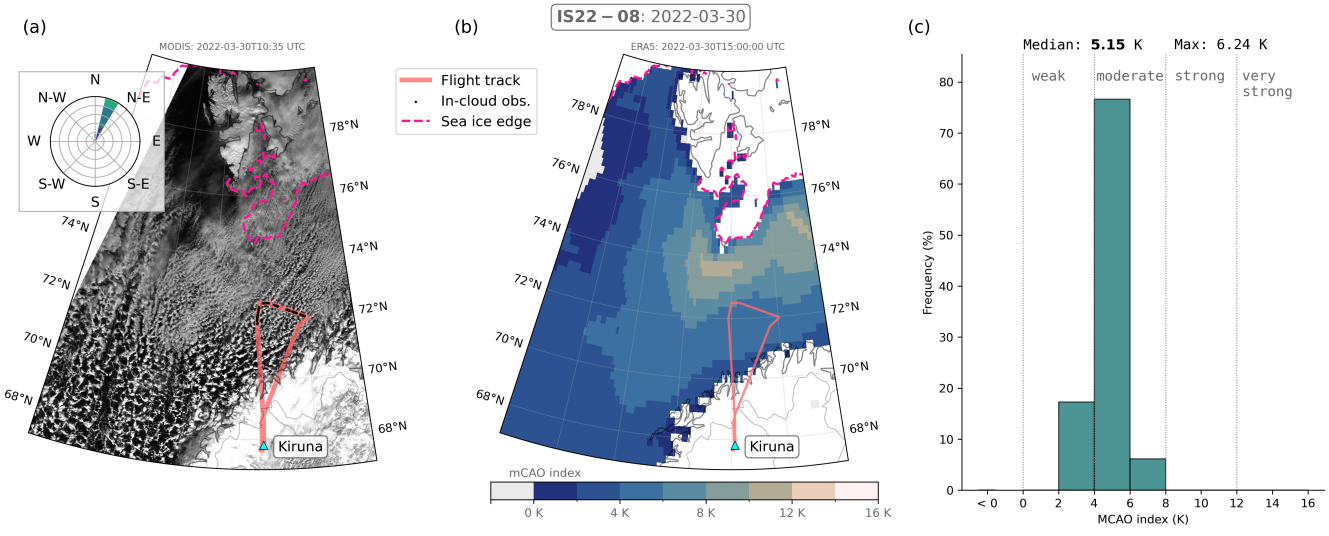

Figure A9. Flight and mCAO information from flight IS22-08. (a) Flight path, MODIS satellite image (Band 1: 620-670 nm wavelenght band), sea ice edge and wind direction. (b) Spatial distribution of mCAO index on day of flight. (c) Histogram of mCAO values along flight track.

https://doi.org/10.5194/egusphere-2026-1650
Preprint. Discussion started: 16 April 2026

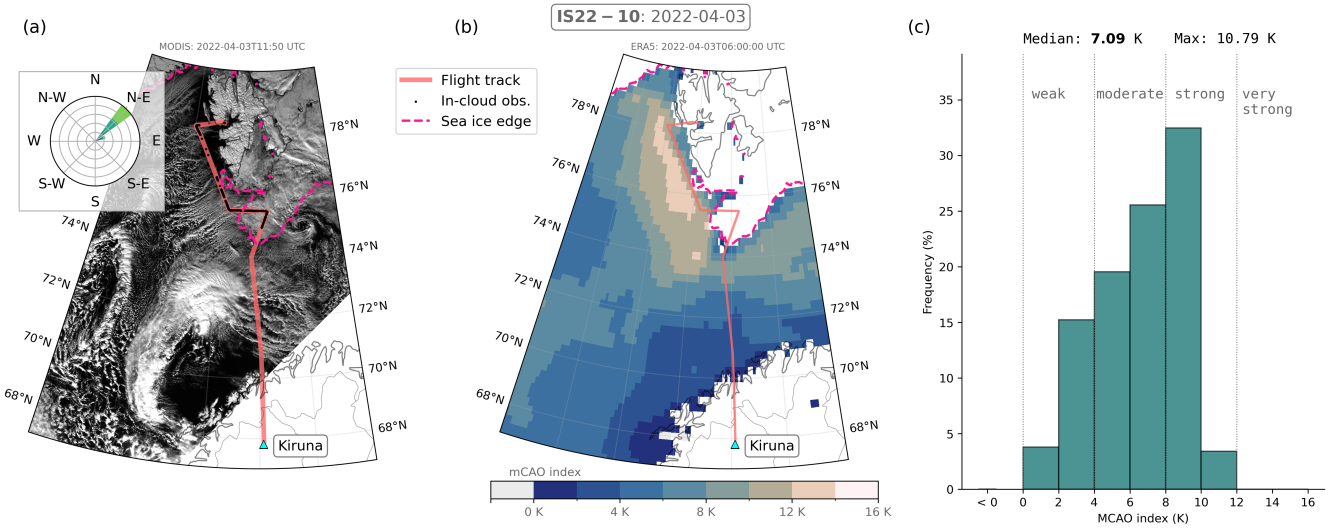

Figure A10. Flight and mCAO information from flight IS22-10. (a) Flight path, MODIS satellite image (Band 1: 620-670 nm wavelenght band), sea ice edge and wind direction. (b) Spatial distribution of mCAO index on day of flight. (c) Histogram of mCAO values along flight track.

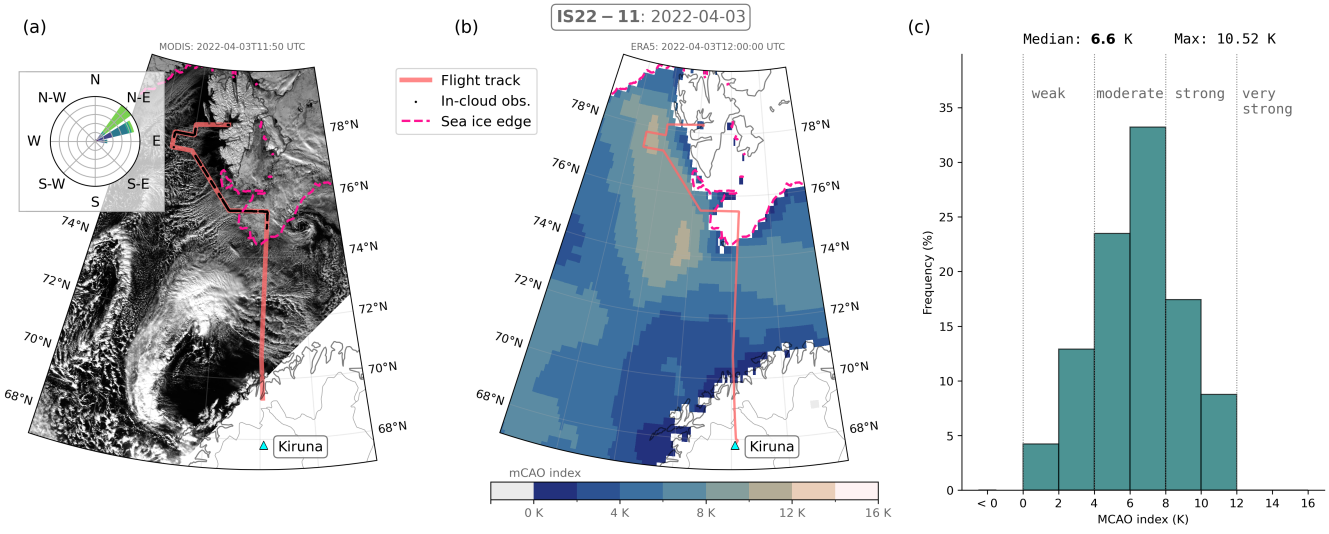

Figure A11. Flight and mCAO information from flight IS22-11. (a) Flight path, MODIS satellite image (Band 1: 620-670 nm wavelenght band), sea ice edge and wind direction. (b) Spatial distribution of mCAO index on day of flight. (c) Histogram of mCAO values along flight track.

https://doi.org/10.5194/egusphere-2026-1650
Preprint. Discussion started: 16 April 2026

Code and data availability. The code used to analyze the in situ data and to produce the figures is available on the public GitHub repository: https://github.com/niellaNina/procIslasMicrophy. The open-source System for OAP Data Analysis (SODA2) is available at https://github.com/abansemer/soda2. The NIMBUS sea ice concentration data is available at https://nsidc.org/data/nsidc-0051/versions/2 (DiGirolamo et al., 2022). The MERRA-2 reanalysis products are accessible at https://disc.gsfc.nasa.gov/datasets/M2T1NXSLV_5.12.4/summary (Global Modeling and Assimilation Office (GMAO), 2015). The MODIS satellite data are available at https://ladsweb.modaps.eosdis.nasa.gov/missions-and-measurements/products/MOD021KM. For the calculation of per-flight mCAO indices, the ERA5 reanalysis data is provided by ECMWF through the Copernicus Climate Change Service (C3S) Climate Data Store (CDS) (Hersbach, H. et al., 2023). The sea ice concentration data used in Figs A3-A11 is from the Institute of Environmental Physics (IUP), University of Bremen, based on the ARTIST Sea Ice (ASI) algorithm (Spreen et al., 2008). The daily data sets (Melsheimer and Spreen, 2019a, b, 2020a, b) were downloaded for the ISLAS2022 period from the data publisher PANGAEA.

Author contributions. NEL, TC, ROD and TS designed the study. NEL post-processed and analysed the dataset with support from ROD and TC. HS, AS and TC were involved in the acquisition of the in situ measurements. TC calculated mCAO indices for each flight, and FSvdL calculated the distances from the sea ice. NEL wrote the paper with contributions from all authors.

Competing interests. The authors declare that they have no conflict of interest.

Acknowledgements. This research was funded by the European Research Council through ERC Consolidator Grant "STEP-CHANGE" (grant number 101045273) and through Grant StG758005, and by the University of Oslo Sustainability Initiative through the "ACT-Pilot" project. ROD ackowledges funding through EU-HORIZON-WIDERA-2021 Grant no. 101079385 (BRACE-MY) and EEA Grants/Norway Grants (grant no. EEARO-NO-2019-0423/IceSafari, contract no. 31/2020). HS acknowledges the European Research Council for funding through Grant Nr. 773245 (ISLAS (Isotopic Links to Atmospheric Water's Sources)). We are grateful for the support received from Aaron Bansemer (NCAR) for setting up SODA2 with the right cloud probe configuration files. Although generative AI was not directly used in the writing of this article, we acknowledge its use in suggesting language formulations.

https://doi.org/10.5194/egusphere-2026-1650
Preprint. Discussion started: 16 April 2026

References

Abel, S. J., Boutle, I. A., Waite, K., Fox, S., Brown, P. R. A., Cotton, R., Lloyd, G., Choularton, T. W., and Bower, K. N.: The Role of Precipitation in Controlling the Transition from Stratocumulus to Cumulus Clouds in a Northern Hemisphere Cold-Air Outbreak, Journal of the Atmospheric Sciences, 74, 2293–2314, https://doi.org/10.1175/JAS-D-16-0362.1, publisher: American Meteorological Society Section: Journal of the Atmospheric Sciences, 2017.

Andronache, C.: Introduction, in: Mixed-Phase Clouds: Observations and Modeling, pp. 1–9, Elsevier, https://doi.org/10.1016/B978-0-12-810549-8.00001-5, 2017.

Aragon, L. G., Crosier, J., Connolly, P., Huang, Y., May, P., and Abel, S.: Characterizing the Shape of Cloud Particle Size Distributions in High-Latitude Marine Cold-Air Outbreaks, Journal of Geophysical Research: Atmospheres, 130, e2024JD043 033, https://doi.org/10.1029/2024JD043033, 2025.

Bansemer, A.: System for OAP Data Analysis (SODA), https://github.com/abansemer/soda2, original-date: 2016-07-22T09:21:04Z, 2016.

Baumgardner, D., Jonsson, H., Dawson, W., O'Connor, D., and Newton, R.: The cloud, aerosol and precipitation spectrometer: a new instrument for cloud investigations, Atmospheric research, 59, 251–264, https://doi.org/10.1016/S0169-8095(01)00119-3, place: NEW YORK Publisher: Elsevier B.V, 2001.

Baumgardner, D., Brenguier, J., Bucholtz, A., Coe, H., DeMott, P., Garrett, T., Gayet, J., Hermann, M., Heymsfield, A., Korolev, A., Krämer, M., Petzold, A., Strapp, W., Pilewskie, P., Taylor, J., Twohy, C., Wendisch, M., Bachalo, W., and Chuang, P.: Airborne instruments to measure atmospheric aerosol particles, clouds and radiation: A cook's tour of mature and emerging technology, Atmospheric Research, 102, 10–29, https://doi.org/10.1016/j.atmosres.2011.06.021, 2011.

Bigg, E. K. and Leck, C.: Cloud-active particles over the central Arctic Ocean, Journal of Geophysical Research: Atmospheres, 106, 32 155–32 166, https://doi.org/10.1029/1999JD901152, 2001.

Brown, P. R. A. and Francis, P. N.: Improved Measurements of the Ice Water Content in Cirrus Using a Total-Water Probe, Journal of Atmospheric and Oceanic Technology, 12, 410–414, https://doi.org/10.1175/1520-0426(1995)012<0410:IMOTIW>2.0.CO;2, publisher: American Meteorological Society Section: Journal of Atmospheric and Oceanic Technology, 1995.

Brümmer, B.: Boundary-layer modification in wintertime cold-air outbreaks from the Arctic sea ice, Boundary-Layer Meteorology, 80, 109–125, https://doi.org/10.1007/BF00119014, company: Springer Distributor: Springer Institution: Springer Label: Springer Number: 1 Publisher: Kluwer Academic Publishers, 1996.

C3S: ERA5 hourly data on single levels from 1940 to present, https://doi.org/10.24381/CDS.ADBB2D47, 2018.

Dahlke, S., Solbès, A., and Maturilli, M.: Cold Air Outbreaks in Fram Strait: Climatology, Trends, and Observations During an Extreme Season in 2020, Journal of Geophysical Research: Atmospheres, 127, e2021JD035 741, https://doi.org/10.1029/2021JD035741, 2022.

Dall´Osto, M., Beddows, D. C. S., Tunved, P., Krejci, R., Ström, J., Hansson, H.-C., Yoon, Y. J., Park, K.-T., Becagli, S., Udisti, R., Onasch, T., O´Dowd, C. D., Simó, R., and Harrison, R. M.: Arctic sea ice melt leads to atmospheric new particle formation, Scientific Reports, 7, 3318, https://doi.org/10.1038/s41598-017-03328-1, 2017.

de Reus, M., Borrmann, S., Bansemer, A., Heymsfield, A. J., Weigel, R., Schiller, C., Mitev, V., Frey, W., and Kunkel, D.: Evidence for ice particles in the tropical stratosphere from in-situ measurements, Atmos. Chem. Phys., 9, p.6775–6792, https://doi.org/DOI: 10.5194/acp-9-6775-2009, 2009.

DiGirolamo, N., Parkinson, C., Cavalieri, D., Gloersen, P., and Zwally, H.: Sea Ice Concentrations from Nimbus-7 SMMR and DMSP SSM/I-SSMIS Passive Microwave Data, Version 2, https://doi.org/10.5067/MPYG15WAA4WX, 2022.

https://doi.org/10.5194/egusphere-2026-1650
Preprint. Discussion started: 16 April 2026

DMT: Cloud Droplet Probe (CDP-2) Operator Manual, Operator manual DOC-0343 Rev A, Droplet Measurement Technologies, 2400 Trad Centre Avenue, Longmont, Colorado, USA 80503, https://dropletmeasure.wpenginepowered.com/wp-content/uploads/2020/02/DOC-0343-Rev-A-CDP-2-Manual.pdf, 2017.

Field, P. R., Heymsfield, A. J., and Bansemer, A.: Shattering and particle interarrival times measured by optical array probes in ice clouds, Journal of atmospheric and oceanic technology, 23, 1357–1371, https://doi.org/10.1175/JTECH1922.1, 2006.

Fletcher, J., Mason, S., and Jakob, C.: The Climatology, Meteorology, and Boundary Layer Structure of Marine Cold Air Outbreaks in Both Hemispheres, Journal of Climate, 29, 1999–2014, https://doi.org/DOI: 10.1175/JCLI-D-15-0268.1, 2016.

Forster, P., Storelvmo, T., Armour, K., Collins, W., Dufresne, J.-L., Frame, D., Lunt, D., Mauritsen, T., Palmer, M., Watanabe, M., Wild, M., and Zhang, H.: The Earth's Energy Budget, Climate Feedbacks, and Climate Sensitivity, in: Climate Change 2021: The Physical Science Basis. Contribution of Working Group I to the Sixth Assessment Report of the Intergovernmental Panel on Climate Change, edited by Masson-Delmotte, V., Zhai, P., Pirani, A., Connors, S., Péan, C., Berger, S., Caud, N., Chen, Y., Goldfarb, L., Gomis, M., Huang, M., Leitzell, K., Lonnoy, E., Matthews, J., Maycock, T., Waterfield, T., Yelekçi, O., Yu, R., and Zhou, B., pp. 923–1054, Cambridge University Press, Cambridge, United Kingdom and New York, NY, USA, https://doi.org/10.1017/9781009157896.009, 2021.

Gayet, J.-F., Stachlewska, I. S., Jourdan, O., Shcherbakov, V., Schwarzenboeck, A., and Neuber, R.: Microphysical and optical properties of precipitating drizzle and ice particles obtained from alternated lidar and in situ measurements, Annales Geophysicae, 25, 1487–1497, https://doi.org/10.5194/angeo-25-1487-2007, 2007.

Geerts, B., Giangrande, S., McFarquhar, G., Xue, L., Abel, S., Comstock, J., Crewell, S., DeMott, P., Ebell, K., Field, P., Hill, T., Hunzinger, A., Jensen, M., Johnson, K., Juliano, T., Kollias, P., Kosovic, B., Lackner, C., Luke, E., Lüpkes, C., Matthews, A., Neggers, R., Ovchinnikov, M., Powers, H., Shupe, M., Spengler, T., Swanson, B., Tjernström, M., Theisen, A., Wales, N., Wang, Y., Wendisch, M., and Wu, P.: The COMBLE Campaign A Study of Marine Boundary Layer Clouds in Arctic Cold-Air Outbreaks, BULLETIN OF THE AMERICAN METEOROLOGICAL SOCIETY, 103, E1371–E1389, https://doi.org/10.1175/BAMS-D-21-0044.1, 2022.

Gelaro, R., McCarty, W., Suárez, M. J., Todling, R., Molod, A., Takacs, L., Randles, C. A., Darmenov, A., Bosilovich, M. G., Reichle, R., Wargan, K., Coy, L., Cullather, R., Draper, C., Akella, S., Buchard, V., Conaty, A., Silva, A. M. d., Gu, W., Kim, G.-K., Koster, R., Lucchesi, R., Merkova, D., Nielsen, J. E., Partyka, G., Pawson, S., Putman, W., Rienecker, M., Schubert, S. D., Sienkiewicz, M., and Zhao, B.: The Modern-Era Retrospective Analysis for Research and Applications, Version 2 (MERRA-2), Journal of Climate, 30, 5419 – 5454, https://doi.org/10.1175/JCLI-D-16-0758.1, 2017.

Global Modeling and Assimilation Office (GMAO): MERRA-2 tavg1_2d_slv_Nx: 2d,1-Hourly,Time-Averaged,Single-Level,Assimilation,Single-Level Diagnostics V5.12.4,, https://doi.org/10.5067/VJAFPLI1CSIV, place: Greenbelt, MD, USA, 2015.

Hersbach, H., Bell, B., Berrisford, P., Biavati, G., Horányi, A., Muñoz Sabater, J., Nicolas, J., Peubey, C., Radu, R., Rozum, I., Schepers, D., Simmons, A., Soci, C., and Dee, D.: ERA5 hourly data on single levels from 1940 to present, https://doi.org/10.24381/CDS.ADBB2D47, 2023.

Heymsfield, A. J. and Parrish, J. L.: A Computational Technique for Increasing the Effective Sampling Volume of the PMS Two-Dimensional Particle Size Spectrometer, Journal of Applied Meteorology and Climatology, 17, 1566–1572, https://doi.org/10.1175/1520-0450(1978)017<1566:ACTFIT>2.0.CO;2, 1978.

Hofer, S., Amory, C., Kittel, C., Carlsen, T., Le Toumelin, L., and Storelvmo, T.: The Contribution of Drifting Snow to Cloud Properties and the Atmospheric Radiative Budget Over Antarctica, Geophysical Research Letters, 48, e2021GL094 967, https://doi.org/10.1029/2021GL094967, 2021.

https://doi.org/10.5194/egusphere-2026-1650
Preprint. Discussion started: 16 April 2026

Hueholt, D. M., Yuter, S. E., and Miller, M. A.: Revisiting Diagrams of Ice Growth Environments, Bulletin of the American Meteorological Society, 103, E2584–E2603, https://doi.org/https://doi.org/10.1175/BAMS-D-21-0271.1, 2022.

Juliano, T. W., Lackner, C. P., Geerts, B., Kosović, B., Xue, L., Wu, P., and Olson, J. B.: Simulating Mixed-Phase Open Cellular Clouds Observed During COMBLE: Evaluation of Parameterized Turbulence Closure, Journal of geophysical research. Atmospheres, 129, e2024JD040 889, https://doi.org/10.1029/2024JD040889, 2024.

Järvinen, E., Nehlert, F., Xu, G., Waitz, F., Mioche, G., Dupuy, R., Jourdan, O., and Schnaiter, M.: Investigating the vertical extent and short-wave radiative effects of the ice phase in Arctic summertime low-level clouds, Atmospheric Chemistry and Physics, 23, 7611–7633, https://doi.org/10.5194/acp-23-7611-2023, 2023.

Karalis, M., Sotiropoulou, G., Abel, S. J., Bossioli, E., Georgakaki, P., Methymaki, G., Nenes, A., and Tombrou, M.: Effects of secondary ice processes on a stratocumulus to cumulus transition during a cold-air outbreak, Atmospheric Research, 277, 106 302, https://doi.org/10.1016/j.atmosres.2022.106302, 2022.

Klingebiel, M., Ehrlich, A., Ruiz-Donoso, E., Risse, N., Schirmacher, I., Jäkel, E., Schäfer, M., Wolf, K., Mech, M., Moser, M., Voigt, C., and Wendisch, M.: Variability and properties of liquid-dominated clouds over the ice-free and sea-ice-covered Arctic Ocean, Atmospheric Chemistry and Physics, 23, 15 289–15 304, https://doi.org/10.5194/acp-23-15289-2023, 2023.

Kolstad, E. W.: Higher ocean wind speeds during marine cold air outbreaks, Quarterly Journal of the Royal Meteorological Society, 143, 2084–2092, https://doi.org/10.1002/qj.3068, 2017.

Komurcu, M., Storelvmo, T., Tan, I., Lohmann, U., Yun, Y., Penner, J. E., Wang, Y., Liu, X., and Takemura, T.: Intercomparison of the cloud water phase among global climate models, Journal of Geophysical Research: Atmospheres, 119, 3372–3400, https://doi.org/10.1002/2013JD021119, 2014.

Korolev, A.: Limitations of the Wegener–Bergeron–Findeisen Mechanism in the Evolution of Mixed-Phase Clouds, Journal of the atmospheric sciences, 64, 3372–3375, https://doi.org/10.1175/JAS4035.1, 2007.

Korolev, A. and Milbrandt, J.: How Are Mixed-Phase Clouds Mixed?, Geophysical research letters, 49, e2022GL099 578–n/a, https://doi.org/10.1029/2022GL099578, 2022.

Korolev, A., McFarquhar, G., Field, P. R., Franklin, C., Lawson, P., Wang, Z., Williams, E., Abel, S. J., Axisa, D., Borrmann, S., Crosier, J., Fugal, J., Krämer, M., Lohmann, U., Schlenczek, O., Schnaiter, M., and Wendisch, M.: Mixed-Phase Clouds: Progress and Challenges, Meteorological Monographs, 58, 5.1–5.50, https://doi.org/10.1175/AMSMONOGRAPHS-D-17-0001.1, publisher: American Meteorological Society Section: Meteorological Monographs, 2017.

Korolev, A. V., Strapp, J. W., and Isaac, G. A.: Evaluation of the Accuracy of PMS Optical Array Probes, Journal of Atmospheric and Oceanic Technology, 15, 708–720, https://doi.org/10.1175/1520-0426(1998)015<0708:EOTAOP>2.0.CO;2, 1998.

Korolev, A. V., Emery, E. F., Strapp, J. W., Cober, S. G., and Isaac, G. A.: Quantification of the Effects of Shattering on Airborne Ice Particle Measurements, Journal of Atmospheric and Oceanic Technology, 30, 2527–2553, https://doi.org/10.1175/JTECH-D-13-00115.1, 2013.

Lackner, C., Geerts, B., Juliano, T., Kosovic, B., and Xue, L.: Characterizing Mesoscale Cellular Convection in Marine Cold Air Outbreaks With a Machine Learning Approach, Journal of Geophysical Research, 129, e2024JD041 651, https://doi.org/10.1029/2024JD041651, 2024.

Lackner, C. P., Geerts, B., Juliano, T. W., Xue, L., and Kosovic, B.: Vertical Structure of Clouds and Precipitation During Arctic Cold-Air Outbreaks and Warm-Air Intrusions: Observations From COMBLE, Journal of Geophysical Research: Atmospheres, 128, e2022JD038 403, https://doi.org/10.1029/2022JD038403, 2023.

https://doi.org/10.5194/egusphere-2026-1650
Preprint. Discussion started: 16 April 2026

Landgren, O. A., Seierstad, I. A., and Iversen, T.: Projected future changes in Marine Cold-Air Outbreaks associated with Polar Lows in the Northern North-Atlantic Ocean, Climate Dynamics, 53, 2573–2585, https://doi.org/10.1007/s00382-019-04642-2, 2019.

Lloyd, G., Choularton, T., Bower, K., Gallagher, M., Crosier, J., O'Shea, S., Abel, S., Fox, S., Cotton, R., and Boutle, I.: In situ measurements of cloud microphysical and aerosol properties during the break-up of stratocumulus cloud layers in cold air outbreaks over the North Atlantic, ATMOSPHERIC CHEMISTRY AND PHYSICS, 18, 17 191–17 206, https://doi.org/10.5194/acp-18-17191-2018, 2018.

Mages, Z., Kollias, P., Zhu, Z., and Luke, E.: Surface-based observations of cold-air outbreak clouds during the COMBLEfield campaign, ATMOSPHERIC CHEMISTRY AND PHYSICS, 23, 3561–3574, https://doi.org/10.5194/acp-23-3561-2023, 2023.

McFarquhar, G. M., Zhang, G., Poellot, M. R., Kok, G. L., McCoy, R., Tooman, T., Fridlind, A., and Heymsfield, A. J.: Ice properties of single-layer stratocumulus during the Mixed-Phase Arctic Cloud Experiment: 1. Observations, Journal of Geophysical Research: Atmospheres, 112, 2007JD008 633, https://doi.org/10.1029/2007JD008633, 2007.

Melsheimer, C. and Spreen, G.: AMSR2 ASI sea ice concentration data, Antarctic, version 5.4 (NetCDF) (July 2012 - December 2019), https://doi.org/10.1594/PANGAEA.898400, 2019a.

Melsheimer, C. and Spreen, G.: AMSR2 ASI sea ice concentration data, Arctic, version 5.4 (NetCDF) (July 2012 - December 2019), https://doi.org/10.1594/PANGAEA.898399, 2019b.

Melsheimer, C. and Spreen, G.: AMSR-E ASI sea ice concentration data, Arctic, version 5.4 (NetCDF) (June 2002 - September 2011), https://doi.org/10.1594/PANGAEA.919777, 2020a.

Melsheimer, C. and Spreen, G.: AMSR-E ASI sea ice concentration data, Antarctic, version 5.4 (NetCDF) (June 2002 - September 2011), https://doi.org/10.1594/PANGAEA.919778, 2020b.

Mioche, G., Jourdan, O., Ceccaldi, M., and Delanoë, J.: Variability of mixed-phase clouds in the Arctic with a focus on the Svalbard region: a study based on spaceborne active remote sensing, Atmospheric Chemistry and Physics, 15, 2445–2461, https://doi.org/10.5194/acp-15-2445-2015, 2015.

Mioche, G., Jourdan, O., Delanoë, J., Gourbeyre, C., Febvre, G., Dupuy, R., Monier, M., Szczap, F., Schwarzenboeck, A., and Gayet, J.: Vertical distribution of microphysical properties of Arctic springtime low-level mixed-phase clouds over the Greenland and Norwegian seas, ATMOSPHERIC CHEMISTRY AND PHYSICS, 17, 12 845–12 869, https://doi.org/10.5194/acp-17-12845-2017, 2017.

Mitchell, D. L., Lawson, R. P., and Baker, B.: Understanding effective diameter and its application to terrestrial radiation in ice clouds, Atmospheric Chemistry and Physics, 11, 3417–3429, https://doi.org/10.5194/acp-11-3417-2011, 2011.

MODIS Science Team: MOD021KM MODIS/Terra Calibrated Radiances 5-Min L1B Swath 1km, https://doi.org/10.5067/MODIS/MOD021KM.061, 2017.

Morrison, H., de Boer, G., Feingold, G., Harrington, J., Shupe, M. D., and Sulia, K.: Resilience of persistent Arctic mixed-phase clouds, Nature Geoscience, 5, 11–17, https://doi.org/10.1038/ngeo1332, 2012.

Moser, M., Voigt, C., Jurkat-Witschas, T., Hahn, V., Mioche, G., Jourdan, O., Dupuy, R., Gourbeyre, C., Schwarzenboeck, A., Lucke, J., Boose, Y., Mech, M., Borrmann, S., Ehrlich, A., Herber, A., Lüpkes, C., and Wendisch, M.: Microphysical and thermodynamic phase analyses of Arctic low-level clouds measured above the sea ice and the open ocean in spring and summer, Atmospheric Chemistry and Physics, 23, 7257–7280, https://doi.org/10.5194/acp-23-7257-2023, 2023.

Murray-Watson, R. J. and Gryspeerdt, E.: Air mass history linked to the development of Arctic mixed-phase clouds, Atmospheric Chemistry and Physics, 24, 11 115–11 132, https://doi.org/10.5194/acp-24-11115-2024, 2024.

https://doi.org/10.5194/egusphere-2026-1650
Preprint. Discussion started: 16 April 2026

Murray-Watson, R. J., Gryspeerdt, E., and Goren, T.: Investigating the development of clouds within marine cold-air outbreaks., Atmospheric Chemistry and Physics, 23, 9365–9365, https://go.gale.com/ps/i.do?p=AONE&sw=w&issn=16807316&v=2.1&it=r&id=GALE%7CA762708132&sid=googleScholar&linkaccess=abs, publisher: Copernicus GmbH, 2023.

Papakonstantinou-Presvelou, I., Sourdeval, O., and Quaas, J.: Strong Ocean/Sea-Ice Contrasts Observed in Satellite-Derived Ice Crystal Number Concentrations in Arctic Ice Boundary-Layer Clouds, GEOPHYSICAL RESEARCH LETTERS, 49, e2022GL098 207., https://doi.org/10.1029/2022GL098207, 2022.

Papritz, L. and Spengler, T.: A Lagrangian Climatology of Wintertime Cold Air Outbreaks in the Irminger and Nordic Seas and Their Role in Shaping Air–Sea Heat Fluxes, Journal of Climate, 30, 2717–2737, https://doi.org/DOI: 10.1175/JCLI-D-16-0605.1, 2017.

Papritz, L., Pfahl, S., Sodemann, H., and Wernli, H.: A Climatology of Cold Air Outbreaks and Their Impact on Air–Sea Heat Fluxes in the High-Latitude South Pacific, Journal of Climate, 28, 342–364, https://doi.org/10.1175/JCLI-D-14-00482.1, 2015.

Peng, Y., Lohmann, U., Leaitch, R., Banic, C., and Couture, M.: The cloud albedo-cloud droplet effective radius relationship for clean and polluted clouds from RACE and FIRE.ACE, Journal of Geophysical Research: Atmospheres, 107, AAC 1–1–AAC 1–6, https://doi.org/10.1029/2000JD000281, 2002.

Pithan, F. and Mauritsen, T.: Arctic amplification dominated by temperature feedbacks in contemporary climate models, Nature Geoscience, 7, 181–184, https://doi.org/10.1038/ngeo2071, 2014.

Pithan, F., Svensson, G., Caballero, R., Chechin, D., Cronin, T. W., Ekman, A. M. L., Neggers, R., Shupe, M. D., Solomon, A., Tjernström, M., and Wendisch, M.: Role of air-mass transformations in exchange between the Arctic and mid-latitudes, Nature Geoscience, 11, 805–812, https://doi.org/10.1038/s41561-018-0234-1, 2018.

Ruiz-Donoso, E., Ehrlich, A., Schäfer, M., Jäkel, E., Schemann, V., Crewell, S., Mech, M., Kulla, B., Kliesch, L., Neuber, R., and Wendisch, M.: Small-scale structure of thermodynamic phase in Arctic mixed-phase clouds observed by airborne remote sensing during a cold air outbreak and a warm air advection event, ATMOSPHERIC CHEMISTRY AND PHYSICS, 20, 5487–5511, https://doi.org/10.5194/acp-20-5487-2020, 2020.

Saggiorato, B., Nuijens, L., Siebesma, A. P., de Roode, S., Sandu, I., and Papritz, L.: The Influence of Convective Momentum Transport and Vertical Wind Shear on the Evolution of a Cold Air Outbreak, Journal of Advances in Modeling Earth Systems, 12, e2019MS001 991, https://doi.org/10.1029/2019MS001991, 2020.

Schirmacher, I., Schnitt, S., Klingebiel, M., Maherndl, N., Kirbus, B., Ehrlich, A., Mech, M., and Crewell, S.: Clouds and precipitation in the initial phase of marine cold-air outbreaks as observed by airborne remote sensing, Atmospheric Chemistry and Physics, 24, 12 823–12 842, https://doi.org/10.5194/acp-24-12823-2024, 2024.

Serreze, M. C. and Barry, R. G.: Processes and impacts of Arctic amplification: A research synthesis, Global and Planetary Change, 77, 85–96, https://doi.org/10.1016/j.gloplacha.2011.03.004, 2011.

Shupe, M. D. and Intrieri, J. M.: Cloud Radiative Forcing of the Arctic Surface: The Influence of Cloud Properties, Surface Albedo, and Solar Zenith Angle, Journal of Climate, 17, 616–628, https://doi.org/10.1175/1520-0442(2004)017<0616:CRFOTA>2.0.CO;2, 2004.

Sodemann, H.: ISotopic Links to Atmospheric water's Sources Spring 2022 campaign (in prep), 2026.

Spanu, A., Dollner, M., Gasteiger, J., Bui, T. P., and Weinzierl, B.: Flow-induced errors in airborne in situ measurements of aerosols and clouds., Atmospheric Measurement Techniques, 13, 1963–1963, https://go.gale.com/ps/i.do?p=AONE&sw=w&issn=18671381&v=2.1&it=r&id=GALE%7CA621127095&sid=googleScholar&linkaccess=abs, 2020.

Spreen, G., Kaleschke, L., and Heygster, G.: Sea ice remote sensing using AMSR-E 89-GHz channels, Journal of Geophysical Research: Oceans, 113, https://doi.org/10.1029/2005JC003384, 2008.

https://doi.org/10.5194/egusphere-2026-1650
Preprint. Discussion started: 16 April 2026

Tan, I. and Storelvmo, T.: Evidence of Strong Contributions From Mixed-Phase Clouds to Arctic Climate Change, Geophysical Research Letters, 46, 2894–2902, https://doi.org/10.1029/2018GL081871, 2019.

Taylor, P. C., Boeke, R. C., Boisvert, L. N., Feldl, N., Henry, M., Huang, Y., Langen, P. L., Liu, W., Pithan, F., Sejas, S. A., and Tan, I.: Process Drivers, Inter-Model Spread, and the Path Forward: A Review of Amplified Arctic Warming, Frontiers in Earth Science, 9, 758 361, https://doi.org/10.3389/feart.2021.758361, 2022.

Tornow, F., Ackerman, A. S., and Fridlind, A. M.: Preconditioning of overcast-to-broken cloud transitions by riming in marine cold air outbreaks, Atmospheric Chemistry and Physics, 21, 12 049–12 067, https://doi.org/10.5194/acp-21-12049-2021, 2021.

Torri, G., Kuang, Z., and Tian, Y.: Mechanisms for convection triggering by cold pools, Geophysical Research Letters, 42, 1943–1950, https://doi.org/10.1002/2015GL063227, 2015.

Wendisch, M., Brückner, M., Crewell, S., Ehrlich, A., Notholt, J., Lüpkes, C., Macke, A., Burrows, J. P., Rinke, A., Quaas, J., Maturilli, M., Schemann, V., Shupe, M. D., Akansu, E. F., Barrientos-Velasco, C., Bärfuss, K., Blechschmidt, A.-M., Block, K., Bougoudis, I., Bozem, H., Böckmann, C., Bracher, A., Bresson, H., Bretschneider, L., Buschmann, M., Chechin, D. G., Chylik, J., Dahlke, S., Deneke, H., Dethloff, K., Donth, T., Dorn, W., Dupuy, R., Ebell, K., Egerer, U., Engelmann, R., Eppers, O., Gerdes, R., Gierens, R., Gorodetskaya, I. V., Gottschalk, M., Griesche, H., Gryanik, V. M., Handorf, D., Harm-Altstädter, B., Hartmann, J., Hartmann, M., Heinold, B., Herber, A., Herrmann, H., Heygster, G., Höschel, I., Hofmann, Z., Hölemann, J., Hünerbein, A., Jafariserajehlou, S., Jäkel, E., Jacobi, C., Janout, M., Jansen, F., Jourdan, O., Jurányi, Z., Kalesse-Los, H., Kanzow, T., Käthner, R., Kliesch, L. L., Klingebiel, M., Knudsen, E. M., Kovács, T., Körtke, W., Krampe, D., Kretzschmar, J., Kreyling, D., Kulla, B., Kunkel, D., Lampert, A., Lauer, M., Lelli, L., Von Lerber, A., Linke, O., Löhnert, U., Lonardi, M., Losa, S. N., Losch, M., Maahn, M., Mech, M., Mei, L., Mertes, S., Metzner, E., Mewes, D., Michaelis, J., Mioche, G., Moser, M., Nakoudi, K., Neggers, R., Neuber, R., Nomokonova, T., Oelker, J., Papakonstantinou-Presvelou, I., Pätzold, F., Pefanis, V., Pohl, C., Van Pinxteren, M., Radovan, A., Rhein, M., Rex, M., Richter, A., Risse, N., Ritter, C., Rostosky, P., Rozanov, V. V., Donoso, E. R., Saavedra Garfias, P., Salzmann, M., Schacht, J., Schäfer, M., Schneider, J., Schnierstein, N., Seifert, P., Seo, S., Siebert, H., Soppa, M. A., Spreen, G., Stachlewska, I. S., Stapf, J., Stratmann, F., Tegen, I., Viceto, C., Voigt, C., Vountas, M., Walbröl, A., Walter, M., Wehner, B., Wex, H., Willmes, S., Zanatta, M., and Zeppenfeld, S.: Atmospheric and Surface Processes, and Feedback Mechanisms Determining Arctic Amplification: A Review of First Results and Prospects of the (AC)3 Project, Bulletin of the American Meteorological Society, 104, E208–E242, https://doi.org/10.1175/BAMS-D-21-0218.1, 2023.

Wu, W. and McFarquhar, G. M.: On the Impacts of Different Definitions of Maximum Dimension for Nonspherical Particles Recorded by 2D Imaging Probes, Journal of Atmospheric and Oceanic Technology, 33, 1057–1072, https://doi.org/10.1175/JTECH-D-15-0177.1, 2016.

Wyser, K. and Yang, P.: Average ice crystal size and bulk short-wave single-scattering properties of cirrus clouds, Atmospheric Research, 49, 315–335, https://doi.org/10.1016/S0169-8095(98)00083-0, 1998.

Young, G., Jones, H., Choularton, T., Crosier, J., Bower, K., Gallagher, M., Davies, R., Renfrew, I., Elvidge, A., Darbyshire, E., Marenco, F., Brown, P., Ricketts, H., Connolly, P., Lloyd, G., Williams, P., Allan, J., Taylor, J., Liu, D., and Flynn, M.: Observed microphysical changes in Arctic mixed-phase clouds when transitioning from sea ice to open ocean, ATMOSPHERIC CHEMISTRY AND PHYSICS, 16, 13 945–13 967, https://doi.org/10.5194/acp-16-13945-2016, 2016.

Young, G. S., Kristovich, D. A. R., Hjelmfelt, M. R., and Foster, R. C.: ROLLS, STREETS, WAVES, AND MORE: A Review of Quasi-Two-Dimensional Structures in the Atmospheric Boundary Layer, Bulletin of the American Meteorological Society, 83, 997–1001, https://doi.org/10.1175/1520-0477(2002)083<0997:rswama>2.3.co;2, 2002.